ISSN 1998-0124 CN 11-5974/O4
https://doi.org/10.26599/NR.2025.94908145

Research Article

Alkynyl-protected Cu_{67} nanocluster superatom: Structure anatomy and electrochemical CO_2 reducion study

Ziyi Liu[1,§], Siqi Li[2,§], Lancheng Zhao[3,§], Lubing Qin[1], Jingwen Yang[1], Tao Wu[1], Likai Wang[3](✉), Qing Tang[2](✉), Zhenghua Tang[1](✉)

[1] New Energy Research Institute, School of Environment and Energy, South China University of Technology, Guangzhou Higher Education Mega Centre, Guangzhou 510006, China

[2] School of Chemistry and Chemical Engineering, Chongqing Key Laboratory of Theoretical and Computational Chemistry, Chongqing University, Chongqing 401331, China

[3] School of Chemistry and Chemical Engineering, Shandong University of Technology, Zibo 255049, China

[§] Ziyi Liu, Siqi Li, and Lancheng Zhao contributed equally to this work.

Nano Res., **Just Accepted Manuscript** • https://doi.org/10.26599/NR.2025.94908145
https://www.sciopen.com/journal/1998-0124 on Oct. 10, 2025

© The Authors(s)

Just Accepted

This is a "Just Accepted" manuscript, which has been examined by the peer-review process and has been accepted for publication. A "Just Accepted" manuscript is published online shortly after its acceptance,which is prior to technical editing and formatting and author proofing. Tsinghua University Press (TUP) provides "Just Accepted" as an optional and free service which allows authors to make their results available to the research community as soon as possible after acceptance. After a manuscript has been technically edited and formatted, and the page proofs have been corrected, it will be removed from the "Just Accepted" web site and published officially with volume and article number (e.g., *Nano Research*, **2025**, *18*, 94906990). Please note that technical editing may introduce minor changes to the manuscript text and/or graphics which may affect the content, and all legal disclaimers that apply to the journal pertain. In no event shall TUP be held responsible for errors or consequences arising from the use of any information contained in these "Just Accepted" manuscripts. To cite this anuscript please use its Digital Object Identifier (DOI®),which is identical for all formats of publication.

Just Accepted

Alkynyl-protected Cu_{67} nanocluster superatom: Structure anatomy and electrochemical CO_2 reduction study

Ziyi Liu[1,†], Siqi Li[2,†], Lancheng Zhao[3,†], Lubing Qin[1], Jingwen Yang[1], Tao Wu[1], Likai Wang[*3], Qing Tang[*2], and Zhenghua Tang*[1]

[1] New Energy Research Institute, School of Environment and Energy, South China University of Technology, Guangzhou Higher Education Mega Center, Guangzhou, 510006, China

[2] School of Chemistry and Chemical Engineering, Chongqing Key Laboratory of Theoretical and Computational Chemistry, Chongqing University, Chongqing, 401331, China

[3] School of Chemistry and Chemical Engineering, Shandong University of Technology, Zibo, Shandong 255049, China

[†] These authors contributed equally to this work.

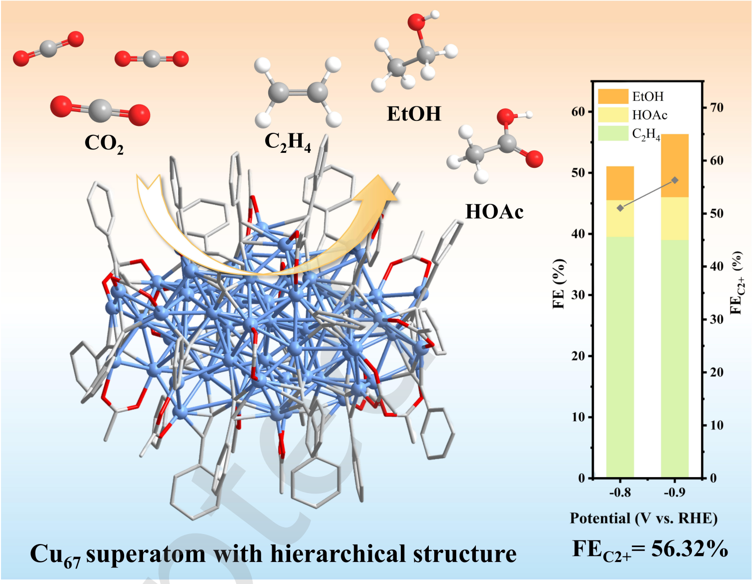

We report a novel Cu_{67} superatom with a hierarchical $Cu_5@Cu_{26}@Cu_{36}$ core, and the Cu core exhibits intrisinc chiral nature but Cu_{67} is a racemate. Cu_{67} displays high selectivity toward C_{2+} products in eCO_2RR, and *in-situ* ATR-SEIRAS discloses the reaction pathway while DFT calculations comprehensively elucidate the reaction mechanism.

Nano Research

ISSN 1998-0124 CN 11-5974/O4
https://doi.org/10.26599/NR.2025.94908145

Alkynyl-protected Cu_{67} nanocluster superatom: Structure anatomy and electrochemical CO_2 reducion study

Ziyi Liu[1,§], Siqi Li[2,§], Lancheng Zhao[3,§], Lubing Qin[1], Jingwen Yang[1], Tao Wu[1], Likai Wang[3] (✉), Qing Tang[2] (✉), and Zhenghua Tang[1] (✉)

[1] *New Energy Research Institute, School of Environment and Energy, South China University of Technology, Guangzhou Higher Education Mega Centre, Guangzhou 510006, China*
[2] *School of Chemistry and Chemical Engineering, Chongqing Key Laboratory of Theoretical and Computational Chemistry, Chongqing University, Chongqing 401331, China*
[3] *School of Chemistry and Chemical Engineering, Shandong University of Technology, Zibo 255049, China*
[§] *Ziyi Liu, Siqi Li, and Lancheng Zhao contributed equally to this work.*

Received: 20 July 2025 / **Revised:** 30 September 2025 / **Accepted:** 10 October 2025

ABSTRACT

Atomically precise high-nuclearity Cu nanoclusters (Cu atom number > 50) with both Cu(I) and Cu(0) species have been rarely reported due to the inherent instability of Cu(0) species. Herein, we report a C_3 symmetric alkynyl-protected $[Cu_{67}(C{\equiv}CPh)_{24}(OAc)_{18}]^-$ (Cu_{67}) superatomic nanocluster, which possesses a hierarchical metal core structure of $Cu_5@Cu_{26}@Cu_{36}$. Cu_{67} is synthesized by a one-pot reduction strategy in which phenylacetylene drive the assembly of a nested architecture stabilized by synergistic μ-coordinated alkynyl ligands (μ_4/μ_5 modes) and κ^2-bridged acetates. Remarkably, when Cu_{67} is used for electrochemical CO_2 reduction reaction (eCO_2RR), deep reduced hydrocarbon chemicals especially the C_{2+} products with high selectivity are acquired. Specifically, Cu_{67} achieves a Faradaic efficiency (FE) of 56.32% for the total C_{2+} products at -0.9 V vs. RHE, among which the FE of ethylene ($FE_{C_2H_4}$) is 39.01%. The excellent catalytic performance from Cu_{67} is superior than most of the recently reported Cu-nanocluster-based catalysts. *In-situ* attenuated total reflection surface-enhanced infrared absorption spectroscopy (ATR-SEIRAS) study reveals the reaction pathway and identifies the key intermediate *COCHO for yielding C_{2+} products. Density functional theory (DFT) calculations systematically elucidate the reaction mechanism of eCO_2RR on Cu_{67} to generate CO and C_2H_4, where the transformation from *CO to *CHO is the rate-determining step for generating the C_{2+} products. This work not only enriches the family member of alkynyl-protected high-nuclearity superatomic Cu nanoclusters, but also provides atomical-level mechanistic insights on employing Cu nanoclusters for eCO_2RR to produce highly valuable products.

KEYWORDS

Cu_{67} nanoclusters, hierarchical structure, electrochemical CO_2 reduction, *in-situ* spectroscopic study, density functional theory calculations

1 Introduction

Electrochemical CO_2 reduction reaction (eCO_2RR) driven by renewable electricity provides an attractive route to close the anthropogenic carbon cycle and acquire valuable carbon-based fuels and feedstocks [1–7]. Particularly, the generation of deep reduced chemicals with higher energy densities such as multi-carbon oxygenate and hydrocarbon products (e. g. C_{2+} molecules, including C_2H_6, C_2H_5OH, C_2H_4, CH_3CHO, CH_3CO_2H, etc.) is highly desired [8–11]. However, the deep reduction and selective conversion of CO_2 into C_{2+} products is highly dependent on the complex reaction conditions especially the catalyst composition and structure. Cu-based nanomaterials have been widely regarded as one of the most effective and promising catalysts that can convert CO_2 into C_{2+} products, thanks to the approriate binding energy to the key intermediates and the strong capability to construct the C-C bonds [12–16]. It is worth noting that, the size, geomertric configuration, local Cu coordination environment, and even the chemical valence state of Cu species can significantly affect the selectivity of C_{2+} products, as C_1 products (e. g. CO, CH_3OH, HCOOH, CH_4) and H_2 are more thermodynamically favorable to be generated simultaneously [17,18]. Therefore, fabricating Cu nanocatalysts with uniform size, precise structure, and homogeneous chemical coordination environment is highly desired for advancing the mechansitic understanding on the structure-activity-selectivty relationship [19–26].

The emergence of molecular Cu nanocluster (Cu NC) with precise structure can potentially resolve the above issue, as these atomically precise Cu nanoclusters possess uniform ultrasmall size (less than 3 nm in diameter) and crystallographically resolved structure [27–31]. In fact, a great deal of research efforts has been dedicated to exploring atomically precise Cu nanoclusters as model and effective catalysts toward eCO_2RR in the past decade. For instance, the Zang and Wang group prepared three Cu clusters of $Cu_8(H)(L_1)_6PF_6$, $Cu_8(^tBuS)_4(L_1)_4$, and $Cu_8(^tBuS)_4(L_2)_4$ with different metal core configurations, and the ditetrahedron-shaped

---

Address correspondence to Zhenghua Tang, zhht@scut.edu.cn; Qing Tang, qingtang@cqu.edu.cn; Likai Wang, lkwangchem@sdut.edu.cn

Cu_8 cluster showed ~2 times Faradaic efficiency (FE) for CO_2-to-HCOOH than the cube-shaped Cu_8 cluster, mainly due to the lower energy barrier to form the key intermediate of HCOO* [32]. In another study, Wu et al. discovered that, the $Cu_6(MBD)_6$ (MBD = 2-mercaptobenzimidazole) cluster with symmetry-broken CuS_2N_1 active sites exhibited a much higher FE toward hydrocarbon products in eCO_2RR than the Cu_6 cluster with symmetric CuS_3 sites. Such performance enhancement is attributed to the asymmetric coordinated CuS_2N_1 sites rearrange the Cu 3d orbitals with d_{x2-y2} as the highest occupied d-orbital, which favors the generation of the key intermediate *COOH for *CO formation [33]. Meanwhile, using $Cu_4(MMI)_4$ and $Cu_8(MMI)_4(^tBuS)_4$ (MMI = 2-mercapto-1-methylimidazole) as model catalytic molecules, Li et al. found the Cu-S dual sites in thiolate-protected Cu nanoclusters play a critical role in accelerating the process of eCO_2RR and water dissociation [34]. Recently, Liu and co-workers invented a co-coupling approach that can realize the hierarchical assembly of Cu(I) nanoclusters, where the Cu_{38} cluster demonstrated outstanding activity in converting CO_2 into hydrocarbon products in eCO_2RR [35]. Note that, Cu nanoclusters can be mainly divided into two types, Cu(I) cluster without valence electrons, and Cu superatomic cluster with valence electrons containing both the Cu(I) and Cu(0) species [36,37]. One may notice that, despite the great progress of employing atomically precise Cu nanoclusters to acquire deep reduced products in eCO_2RR, most of the reported cases are Cu(I) clusters with nuclearity less than 50. Rare case can be found on employing superatomic Cu nanoclusters with more than 50 Cu atoms for eCO_2RR. On one hand, previous studies on Cu nanocatalysts have revealed that, the Cu(0) species can be crucial for enhancing the selectivity of the C_{2+} products [38,39]. On the other hand, relatively larger Cu nanoclusters with over 50 Cu atoms in the core can provide more favorable adjacent sites and surface curvature for the key C-C coupling step for yielding the C_{2+} products [40–42]. Therefore, exploring Cu superatomic nanoclusters with high nulcearity as model catalysts for eCO_2RR is of significant fundamental interests hence being highly desirable.

Meanwhile, despite several cases of high-nuclearity Cu nanoclusters (Cu atom number > 50) have been documented, most of them are rather Cu(I) clusters but not Cu superatoms. For instance, Sagadevan et al. fabricated a $[Cu_{61}(S^tBu)_{26}S_6Cl_6H_{14}]$ cluster (Cu_{61}), which enabled the C−N bond-forming reactions of aryl chlorides under visible-light irradiation [43]. Yan et al. synthesized $Cu_{62}(4\text{-}F\text{-}PhS)_{30}(CF_3COO)_8(PPh_3)_6H_{10}$ for near-infrared photothermal conversion. Under 808 nm laser irradiation, the cluster solution elevated from room temperature to approximately 90°C within 10 mins, achieving a photothermal conversion efficiency of 55.98% [44]. Following that, the same team reported the synthesis of a $[Cu_{58}H_{20}PET_{36}(PPh_3)_4]^{2+}$ nanocluster (Cu_{58}), which can be transformed into surface-defective $[Cu_{57}H_{20}PET_{36}(PPh_3)_4]^+$ cluster (Cu_{57}), and the latter one showed promising activity for click chemistry especially the photoinduced [3+2] azide-alkyne cycloaddition [45]. In another study, the Zang group deeply analyzed the metal packing mode and molecular assembly of $[Cl@Cu_{70}H_{22}(PhC{\equiv}C)_{29}(CF_3COO)_{16}]^{2+}$ (Cu_{70}) [46]. In 2024, Sun et al. recorded the $[Cu_{66}Cl_8(PPh_3)_8(SC_2H_5)_{32}H_{24}]^{2+}$ cluster (Cu_{66}) with hierarchical square motifs, and such Cu_{66} cluster exhibited high catalytic activity and moderate stability in the chemoselective hydrogenation of cyclohexanone [47]. Recently, the Sun and Wang group prepared two robust Cu(I)-alkyne nanoclusters of $[(C_2)_8@Cu_{50}]$ (Cu_{50}) and $[(C_2)_{10}@Cu_{56}]$ (Cu_{56}), and Cu_{50} displays strong yellow phosphorescence and prominent X-ray-excited luminescence [48]. In the above cases, only Cu_{61} is superatomic nanocluster, while Cu_{58}, Cu_{57}, Cu_{70}, Cu_{66}, Cu_{50}, and Cu_{56} are all Cu(I) clusters. Herein, we report an alkynyl-protected high-nuclearity Cu NC superatom of $[Cu_{67}(C{\equiv}CPh)_{24}(OAc)_{18}]^-$ (abbreviated as Cu_{67}) with C_3 symmetry, which exhibits excellent C_{2+} product selectivity in eCO_2RR. Single crystal X-ray diffraction (SC-XRD) analysis reveals that, Cu_{67} adopts a distinctive hierarchical assembled structure comprising an inner Cu_5 hexahedral kernel, a middle layer of eight Cu_3 triangular units with 2 Cu atoms on the C_3 axis, and an outermost layer of twelve Cu_3 units forming a $Cu_5@Cu_{26}@Cu_{36}$ core. In the eCO_2RR test, Cu_{67} can achieve a total hydrocarbon FE of 64.03% at -0.9 V vs. RHE, of which 56.32% is contributed by the C_{2+} products (C_2H_4: 39.01%; CH_3COOH: 7.02%; C_2H_5OH: 10.29%). *In-situ* attenuated total reflection surface-enhanced infrared absorption spectroscopy (ATR-SEIRAS) study identifies the key intermediates and unravels the reaction pathway for generating the C_{2+} products. Further DFT calculations systematically elucidate the reaction mechanism, and confirms the transformation from *CO to *CHO is the rate determining step for yielding the C_{2+} products.

2 Experimental section

See experimental details in Electronic Supplementary Materials.

3 Results and discussion

3.1 Synthesis and structure anatomy of Cu_{67} nanocluster

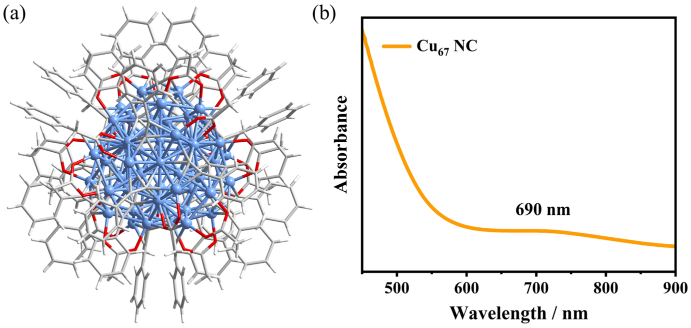

Figure 1 (a) The overall structure of Cu_{67}. (b) Absorbance spectrum of Cu_{67}.

The typical synthesis of Cu_{67} NCs involves the formation of a copper-alkynyl complex followed by a one-pot reduction process, as illustrated in Scheme S1. Initially, copper(I) acetate (Cu(OAc)) and phenylacetylene were mixed together and kept stirring in dichloromethane (DCM) to form the $[Cu(C{\equiv}CPh)]_n$ precursor. Subsequently, diphenylsilane dissolved in DCM was dropwise added under vigorous stirring, and the reaction was allowed to proceed for 9 h, yielding a dark brown crude product. After centrifugation, the solid residue was discarded, and the supernatant was collected. Rotary evaporation was then employed to remove all the solvent, and the resulting solid was acquired after washing by *n*-hexane serveral times. The final product was dissolved in toluene, and black hexagonal block crystals were obtained through hexane diffusion into the toluene solution over 7 days (Figure S1).

The CCDC number for the $[Cu_{67}(C{\equiv}CPh)_{24}(OAc)_{18}]^-$ crystal is 2417379.

Single-crystal X-ray diffraction analysis (SC-XRD) was employed to determine the precise molecular structure of Cu_{67} NC (Figure S2). The detailed crystallographic parameters are summarized in Table S1. The results reveal that, each unit cell contains two cluster molecules (Figure S3), and the molecular formula of the cluster is identified as $[Cu_{67}(C{\equiv}CPh)_{24}(OAc)_{18}]^-$ with a trigonal space group of *P*-31c. The overall structure of Cu_{67} NC shows that, it comprises 67 Cu atoms, 24 phenylacetylene ligands, and 18 acetate ligands (Figure 1a and Figure S4). The UV-vis absorbance spectrum of Cu_{67} in DCM exhibits a broad absorption peak at 690 nm (Figure 1b), an indicative of the characteristic feature. Such absorbance feature is distinctly different from most of the reported high-nuclearity Cu nanoclusters especially the Cu(I) clusters, and it probably originates from the unique hierarchical Cu core structure of Cu_{67} (Table S2). In addition, the absorbance spectra showed that no decomposition of Cu_{67} was observed after one week, indicating the good integrity and stability of the Cu_{67} structure (Figure S5).

To validate the presence of hydride in Cu_{67}, ^{1}H NMR test was conducted and the results are shown in Figure S6. The single peak with chemical shift value at 1.52 ppm can be attributed to water molecule (from the solvent), while the peaks with chemical shift values at 1.27 and 0.87 ppm correspond to hexane. There is a single peak with chemical shift at ~2.00 ppm, which is attributed from the $-CH_3$ group in the OAc ligand. Meanwhile, the peaks with chemical shift values at ~7.39, ~7.13, ~6.94 ppm are from the protons in the o-, m-, -p position of the phenyl groups in the alkynyl ligand. As the integrated area of the NMR peak indicates the stoichiometric ratio, the ratio of 48: 24: 48: 54 agrees well with the cluster formula of $[Cu_{67}(C{\equiv}CPh)_{24}(OAc)_{18}]^-$. It indicates no hydride is present in the Cu_{67} cluster. No counterions were detected in the crystal lattice. To determine the oxidation state of Cu_{67}, ESI-MS measurements were performed, including both positive and negative modes. Molecular ion peaks were observed in both modes, but the peaks in the negative mode were more fragmented. In the positive ion mode, peaks closely resembling the target compound were observed, separated by m/z = 0.5 and bearing a surface charge of +2. Figure S7 shows the peak with m/z at 3907.1305 Da was assigned to $[Cu_{67}(C{\equiv}CPh)_{24}(OAc)_{17}{+}2Cu]^{2+}$ (cal. 3907.1386 Da). Additionally, a peak with m/z at 3969.0979 Da could be fitted to $[Cu_{67}(C{\equiv}CPh)_{24}(OAc)_{18}{+}3Cu]^{2+}$ (Figure S8). It clarifies the oxidation state of the Cu_{67} NC and further confirms the absence of hydrides in the cluster.

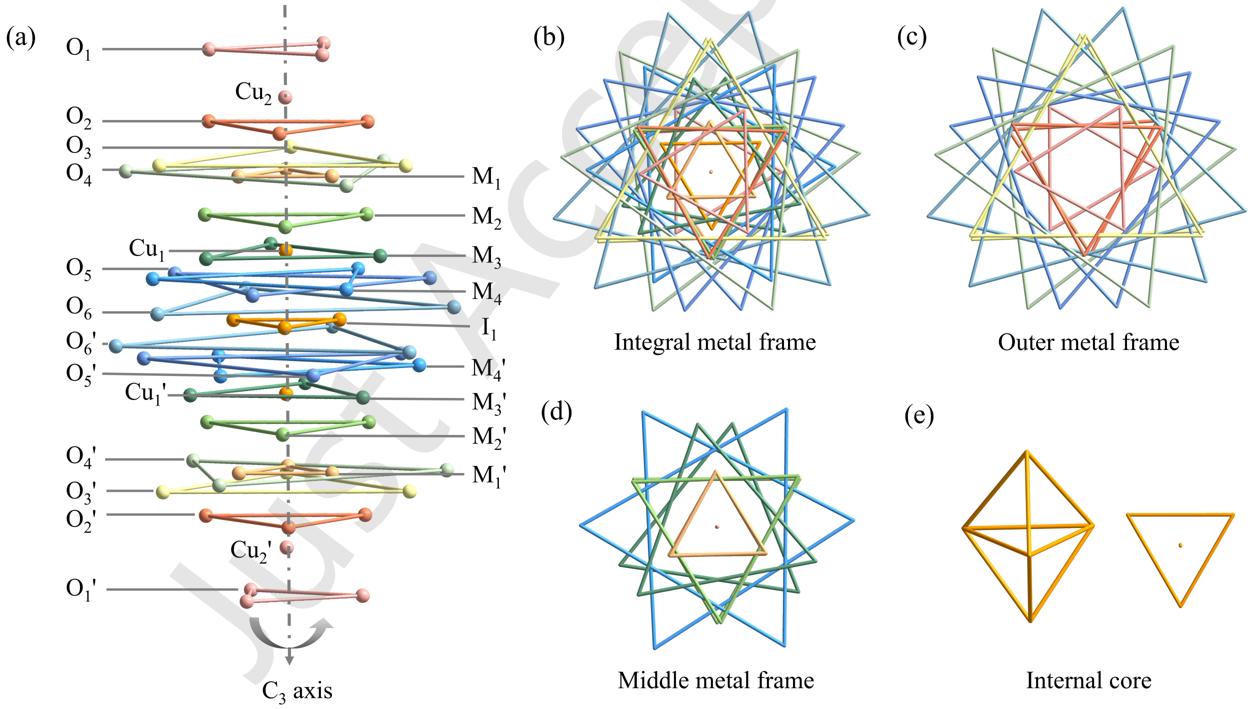

Figure 2 Structure anatomy of the Cu_{67} core. (a) Layer-by-layer display of 67 Cu atoms. (b) Integral metal frame of Cu_{67}. (c) Outer metal frame of Cu_{67}. (d) Middle metal frame of Cu_{67}. (e) Internal core of Cu_{67}.

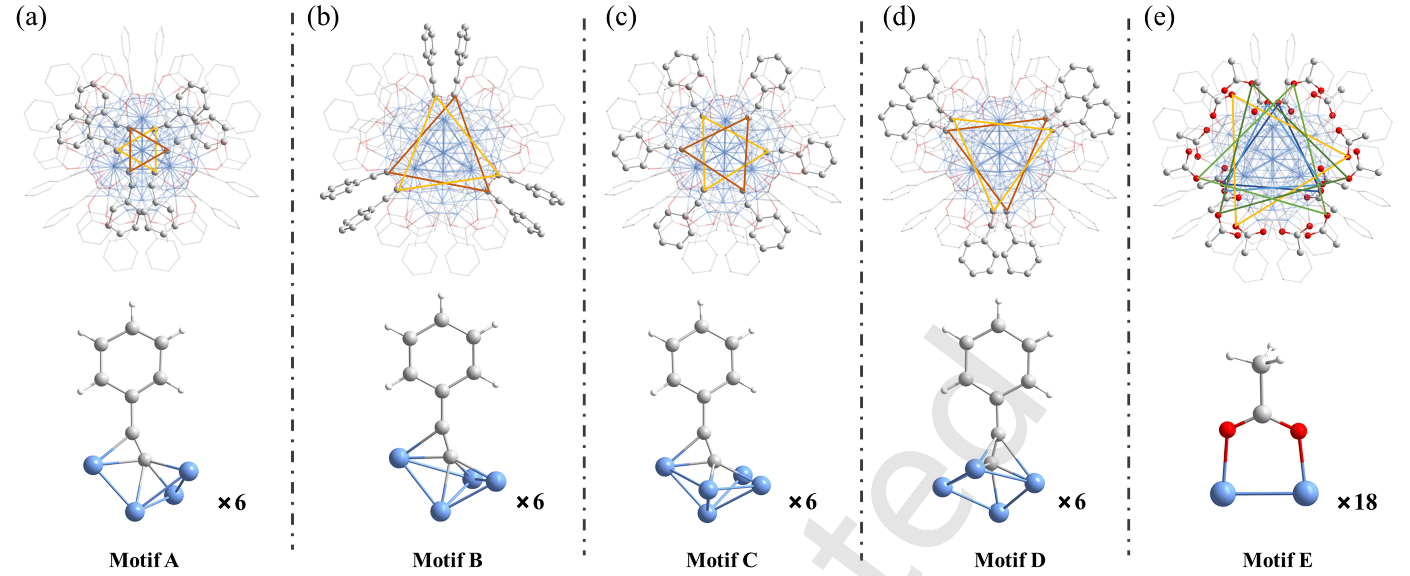

Figure 3 Anatomy of the ligand distribution of Cu_{67}. Resolution of the coordination of (a) motif A, (b) motif B, (c) motif C, (d) motif D, and (e) motif E, as well as the distribution on Cu_{67} in top view along the C_3 axis. Color labels: Cu: blue; O: red; C: gray; H: white.

X-ray photoelectron spectroscopy (XPS) was then utilized to probe the chemical states of the Cu_{67} NC. The survey-scan spectra validated the presence of the Cu, C, O elements (Figure S9a). Meanwhile, the core-level XPS spectra of Cu 2p show two pronounced peaks with binding energies at 932.6 and 952.4 eV, which can be attributed to Cu $2p_{3/2}$ and Cu $2p_{1/2}$, respectively (Figure S9b). As the binding energy of Cu $2p_{3/2}$ is in the between of Cu(I) (~933.1 eV) and Cu(0) (~931.3 eV), it can be speculated the Cu elements in Cu_{67} NC comprise both the Cu(I) and Cu(0) species [49,50]. Meanwhile, the Cu Auger electron spectrum (Figure S9c) shows a shoulder band at 918.5 eV associated with the Cu(0) species, supporting the partial zero valence state of Cu in Cu_{67}, while a main peak at 916.0 eV corresponds to the Cu(I) component. Furthermore, the Cu K-edge X-ray absorption near-edge structure (XANES) spectra in Figure S10 shows consistent results with the Cu Auger spectrum regarding the valence state of Cu. The edge position of Cu_{67} lies between that of Cu_2O (8982.98 eV) and Cu box (8981.07 eV), indicating that the average oxidation state in Cu_{67} is between +1 and 0.[51] In summary, Cu_{67} is a superatomic cluster containing valence electrons, rather than a Cu(I) cluster or complex.

Next, the crystal structure of Cu_{67} is carefully examined. Cu_{67} exhibits a high degree of C_3 symmetry, with an assembly pattern that can be visualized as a stacking of multiple Cu_3 triangles, as depicted in Figure 2a. Additionally, four Cu atoms are positioned along the C_3 axis. The Cu-Cu bond lengths in Cu_{67} range from 2.253(4) Å to 3.092(3) Å, with an average value of 2.643 Å, comparable to the distance in bulk Cu (2.556 Å). A detailed structural analysis reveals a core-shell architecture of the Cu_{67} core, denoted as $Cu_5@Cu_{26}@Cu_{36}$ (Figures 2b-e). The innermost layer consists of a Cu_3 triangle (I_1) and two Cu atoms (Cu_1 and Cu_1', forming a hexahedral Cu_5 kernel. This innermost Cu kernel is ligand-free, with an average Cu-Cu bond length of 2.734 Å. The middle layer comprises eight Cu_3 triangles (M_1, M_1', M_2, M_2', M_3, M_3', M_4, M_4') and two Cu atoms (Cu_2 and Cu_2') located on the C_3 axis. The side length of $M_1(M_1')$, $M_2(M_2')$, $M_3(M_3')$, $M_4(M_4')$ triangles is 2.600 Å, 4.496 Å, 4.894 Å, and 6.415 Å (Not bond length), respectively. The outermost layer is composed of twelve stacked Cu_3 triangles (O_1, O_1', O_2, O_2', O_3, O_3', O_4, O_4', O_5, O_5', O_6, O_6'), with side length of 3.656 Å, 4.430 Å, 6.867 Å, 7.759 Å, 7.274 Å, and 8.473 Å (Not bond length), respectively. The outer Cu atoms are interconnected to form a cocoon-like structure (Figure S11), which has less lateral curvature. Such structural feature may favor the coupling of C-C bonds in eCO_2RR, thus promoting the generation of C_{2+} products.

The metal core configuration of Cu_{67} is then anatomized profoundly in another aspect. As illustrated in Figure S12, the middle layer of Cu_{26} can be divided as two Cu_{13} moieties, which symmetrically bonds to the two sites of the Cu_5 kernel, forming a $Cu_5@Cu_{26}$ centrosymmetric core. The outermost Cu_{36} can be viewed as two pinwheel-shaped Cu_{12} moieties which separately dock onto the Cu_{13} moiety, plus six Cu_2 units that are capped on the middle waist. Interestingly, the six groups of Cu_2 units display two different configurations, where the Cu_2-α unit (connected to motif B, will be discussed in next paragraph) has a torsion angle of ~37° with respect to the C_3 axis, and the Cu_2-β unit (connected to motif D, will be discussed in the next paragraph) has a torsion angle of ~64° (Figure S13). However, as both clockwise and anti-clockwise crossed arrangments are equally present, the Cu_{67} crystal has the equal amount of two entiomers, hence the Cu_{67} cluster is a racemate (Figure S14). Similar phenonmena have also been observed in other coinage metal nanoclusters [52–54].

Subsequently, the spatial configuration and the ligand-metal binding motifs in Cu_{67} are analyzed. The surface ligands of Cu_{67} NC also exhibit a C_3 symmetric distribution. As illustrated in Figures 3a-d, the phenylacetylene ligand presents four distinct coordination modes with the Cu atoms. Specifically, Motif A and Motif B are coordinated by a mode of μ_4: η^1, η^1, η^1, η^2; Motif C by μ_5: η^1, η^1, η^1, η^1, η^2; and Motif D by μ_4: η^1, η^1, η^2, η^2. Motif A and Motif B differ only slightly, with an additional Cu-Cu bond bearing a length of 3.092(3) Å in Motif B; while the corresponding two Cu atoms in Motif A are not bonded due to a large distance of 3.656 Å between them (Figure S15). Each of the four motifs contains six ligands, each forming two L_3 triangles (L = phenylacetylene) bound to the metal core. The positions of the side-view distributions can be found in Figure S16. The 18 acetate ligands bind to the Cu core in a κ^2 coordination mode, which can probably enhance the overall stability of the nanoclusters (Figure 3E). It can be noted that, the alkynyl ligand significantly enriches the coordination modes on the Cu_{67} core surface, where some of these Cu-alkynyl binding motifs have been recorded in previous studies [55–57]. These unique structural features of Cu_{67}, including its multilayered core-shell structure and specific metal-ligand coordination mode, can play a crucial role in determining its physical and chemical properties, paving the way for further exploration of its potential applications.

Moreover, the thorough comparison of atomically precise high-nuclearity Cu nanoclusters (Cu atoms > 50) including the Cu valence, core configuration, symmetry, and main ligand coordination mode are summarized in Table S2. It can be noted that, Cu_{67} is a rare superatom with unique structural feature.

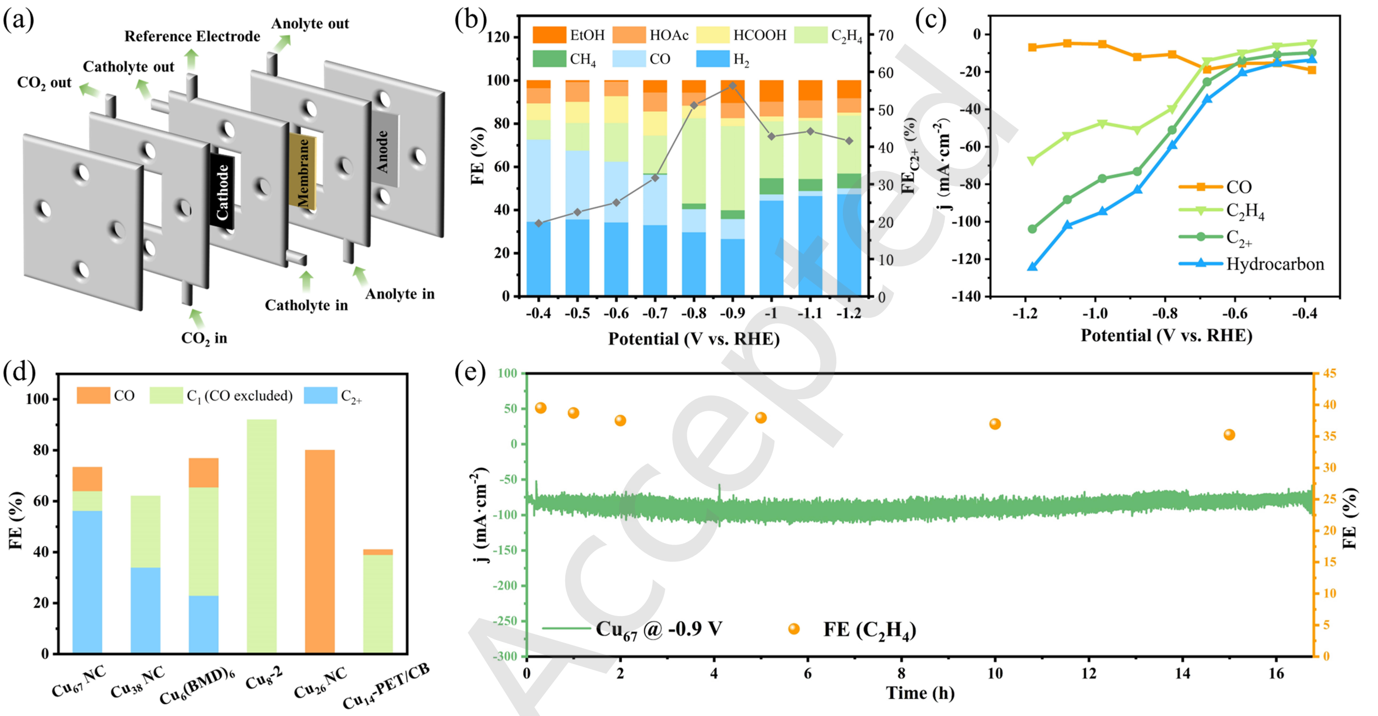

Figure 4 (a) Schematic illustration of eCO_2RR in a gas-fed flow cell. (b) FE values of eCO_2RR products on Cu_{67} at different potentials. (c) Partial current densities of CO, C_2H_4, C_{2+} and hydrocarbons on Cu_{67}. (d) Comparison of eCO_2RR performance of Cu_{67} with reported Cu NCs. (e) Stability test of Cu_{67} at −0.9 V vs. RHE for 17 h.

3.2 eCO_2RR performance of Cu_{67} NC

The catalytic performance of Cu_{67} toward eCO_2RR was then evaluated using a three-compartment flow cell containing a Pt foil as the counter electrode, an Ag/AgCl electrode as the reference electrode, and a nanocluster catalyst-modified carbon paper as the working electrode in 1 M KOH electrolyte (Figure 4a). The linear scanning voltammetry (LSV) curves (Figure S17) reveals that, in a CO_2-saturated electrolyte, the onset overpotential is lower and the measured current density is significantly higher than that in N_2-saturated electrolyte in the presence of Cu_{67} NC. It indicates that, Cu_{67} NC is catalytic effective for eCO_2RR. The gas-phase and liquid-phase products of eCO_2RR are further analyzed by gas chromatography and ^1H NMR spectroscopy, and the detected products include H_2, CO, CH_4, C_2H_4, HCOOH, CH_3COOH, and C_2H_5OH. Figure 4b shows the distribution of the products in the potential range of -0.4 V to -1.2 V (vs. RHE). At -0.4 V, CO is the main product with a FE of 38.06%. As the applied potential goes more negatively, the FE_{CO} gradually decreases to 2.77% at -1.2 V, and the FE of other hydrocarbon products gradually increases, with ethylene being the dominant product. It reaches the maximum FE_{C2H4} value of 39.52% at -0.8 V vs. RHE. The FE_{C2+} reaches the highest value of 56.32% at -0.9 V vs. RHE (C_2H_4: 39.01%; CH_3COOH: 7.02%; C_2H_5OH: 10.29%). At -0.9 V, the FE of the total hydrocarbons is 64.03%, indicating significantly higher selectivity for the C_{2+} products than for the C_1 products (CO excluded).

The partial current density plots (Figure 4c) further corroborate the above conclusion, as the partial current densities of ethylene, C_{2+} products and hydrocarbons increases gradually with the increasing of the applied potential, whereas the partial current density of CO exhibits some fluctuation but decreases in an overall trend. Furthermore, such outstanding catalytic activity in eCO_2RR especially the high FE of the C_{2+} products is superior than most of the recently reported Cu-nanocluster-based catalysts, as summarized in Figure 4d [32,33,35,58,59]. Surprisingly, to the best of our knowledge, no case of high-nuclearity Cu NC superatom to achieve such an excellent FE_{C2+} in eCO_2RR has been reported so far. Furthermore, the long-term stability is another critical descriptor to evaluate the intrinsic catalytic property of an eCO_2RR

catalyst. Notably, Cu_{67} NC exhibits remarkable stability in continuous electrolysis testing over 17 h, with no decay in total current density and maintains stable FE_{C2H4} being above 35% (Figure 4e), suggesting excellent stability for prolonged operation. Additionally, the XPS measurement of Cu_{67} after the stability test was conducted. The complete XPS spectrum (Figure S18a) identified the presence of Cu, C, and O elements, confirming that the core elemental composition of Cu_{67} remained unchanged. As demonstrated in Figure S18b, the binding energies of Cu2p (Cu $2p_{3/2}$ = 932.8 eV; Cu $2p_{1/2}$ = 952.7 eV) exhibited a negligible shift compared to the pre-reaction state, but remained strictly within the typical range of Cu(0) (~931.3 eV) and Cu(I) (~933.1 eV). It strongly validates the electronic stability of Cu_{67}, further confirming its robust catalytic stability.

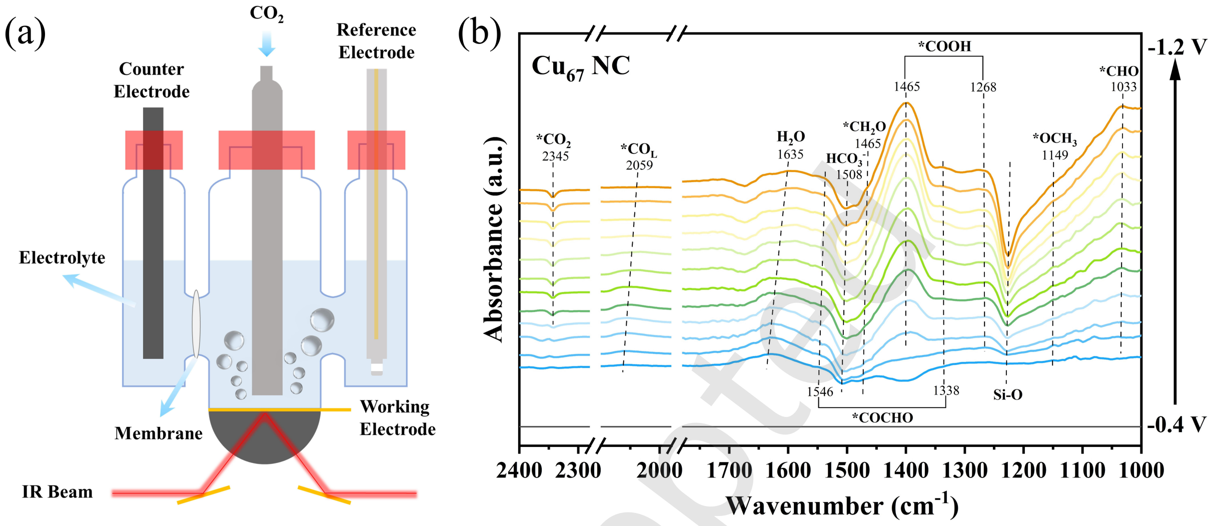

Figure 5 (a) Schematic of the *in-situ* ATR-SEIRAS device. (b) *In-situ* ATR-SEIRAS spectra of Cu_{67} with the applied potential from -0.4 to -1.2 V vs. RHE.

3.3 Mechanistic investigation of eCO_2RR

To deeply comprehend the eCO_2RR mechanism on Cu_{67}, the adsorbed intermediates during the catalytic process are tracked using *In-situ* attenuated total reflection surface enhanced infrared absorption spectroscopy (ATR-SEIRAS). The test setup is shown schematically in Figure 5a, where the electrolyte is a $KHCO_3$ solution saturated with CO_2. As shown in Figure 5b and Figure S19, significant $*CO_2$ adsorption peaks are observed at 2345 cm^{-1}, and the peak at 2059 cm^{-1} corresponds to the CO linear adsorption ($*CO_L$) intermediate, which is a highly reactive intermediate in the eCO_2RR process [60,61]. The $*CO_L$ intermediate can either readily to be protonated to form *CHO or undergoes a coupling reaction to form the key intermediate of *COCHO for generating the C_{2+} products [62]. Meanwhile, the pronounced peaks at 1268 cm^{-1} and 1465 cm^{-1} are attributed to the *COOH intermediate [63], suggesting that CO_2 reduction follows the reaction path of $*CO_2 \rightarrow *COOH \rightarrow *CO$ under high potential conditions. However, as the applied potential goes more negatively, the $*CO_L$ peaks gradually disappear and the characteristic peaks of other intermediates such as *CHO (1033 cm^{-1}), $*OCH_3$ (1149 cm^{-1}), $*CH_2O$ (1465 cm^{-1}) and *COCHO (1338 cm^{-1} and 1546 cm^{-1}) appear successively [34,64–66]. The peaks of $*OCH_3$ and $*CH_2O$ are less pronounced, which is in echo with the lower FE_{C1} value (CO excluded) in eCO_2RR. It indicates that, during the eCO_2RR process, the *CO species undergo further conversion into hydrocarbon-adsorbed species on the Cu_{67} surface, ultimately generating deeply reduced products. Note that, the emergence of the *COCHO peak signifies the initiation of generating the C_{2+} products [67]. Moreover, a distinct, broad peak is observed at 1635 cm^{-1}, corresponding to the OH-vibration band of the adsorbed H_2O. The gradual weakening of this peak suggests that, the H_2O molecule is being activated and subsequently consumed to provide protons for the proton-coupled electron transfer (PCET) process, resulting in the formation of hydrocarbon-adsorbed species with *CO [68]. The above ATR-SEIRAS results offer criticial information for the key intermediate formation, which discloses the general pathway of eCO_2RR to generate both C_1 and C_{2+} products catalyzed by Cu_{67}.

It is also worth noting that, in the overall *in-situ* ATR-SEIRAS spectrum, no Cu-H peak (2090 cm^{-1}) was detected[22]. As such signal is either from the Cu-H bonds in the cluster or due to the cluster adsorbs hydrogen during the electrocatalytic process, it further confirms that Cu_{67} does not structurally contain hydride.

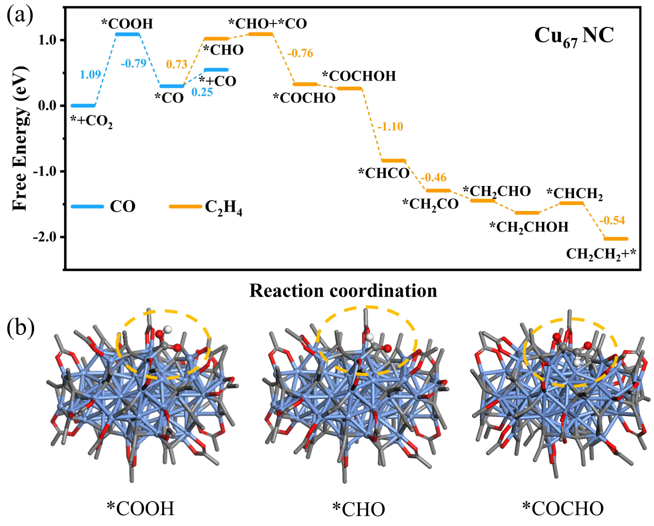

Figure 6 (a) Free-energy diagrams for C_2H_4 and CO formation on Cu_{67} at zero applied potential. (b) Partial critical intermediate configurations. Color labels: Cu: blue; O: red; C: gray; H: white.

To understand the electrocatalytic mechanism over the Cu_{67} NC, we performed DFT calculations to determine the optimal catalytic sites and compare the catalytic selectivity for CO_2 electroreduction to CO versus to C_2H_4. To save the computational cost, we replaced the C≡C-Ph group with C≡C-CH_3 group. The coordinates of the Cu_{67} nanocluster can be found in Table S3. A critical step in enhancing the electrocatalytic activity of nanoclusters is the removal of surface ligands. For Cu_{67}, we removed the alkynyl ligand in order to create the active Cu site (Figure S20). Analysis of the active catalytic sites revealed that, they are located in the low-curvature region at the cluster center. This specific structural feature shortens the distance between adjacent adsorbed intermediates (*CHO and *CO), providing a favorable environment for the C-C coupling reaction in eCO_2RR. The DFT details can be found in Electronic Supplementary Material. The possible pathways for the formation of C_2H_4 are shown in Figure S21. Figure 6a shows the most feasible pathways for reducing CO_2 to CO and C_2H_4 on Cu_{67}. The corresponding intermediate configurations to form CO and C_2H_4 are presented in Figure 6b and Figure S22. We focus on the rate-determining steps (RDS) for the generation of CO and C_2H_4. For the CO_2 to CO conversion, the transformation of * to *COOH is identified as the RDS, exhibiting a free energy barrier of 1.09 eV. For the CO_2 to C_2H_4 conversion, The transformation of *CO to *CHO is identified as the RDS, exhibiting a relatively low free energy barrier of 0.73 eV. The formation of the critical intermediate *COCHO has a negative Gibbs free energy of -0.76 eV. Subsequently, The hydrogenation of *COCHO produces intermediates such as *COCHOH and *CHCO which all have negative Gibbs free energies.

In addition, a systematic study of the stability of key intermediates was conducted, with three representative configurations selected for analysis: *COOH, *CHO+CO, and *COCHO. Most intermediates adsorb on copper sites in a bridging adsorption configuration, as shown in Figure S23a. This adsorption mode favors their stability. Further structural analysis indicates that the bonds formed between the adsorbed intermediates and Cu sites are relatively short (bond lengths ranging from 1.94–2.19 Å), providing a structural basis for the stable existence of the intermediates. Additionally, we performed Hirshfeld charge calculations (Figure S23b), and the results of the charge distribution calculations further confirm the transfer of electrons from the Cu active sites to the adsorbed intermediates, indicating strong interactions between the two. This electron transfer effect not only enhances the adsorption strength between the Cu sites and the intermediates but also confirms the stability of the intermediates in this system at the electronic level.

4 Conclusions

In summary, an atomically precise superatomic high-nuclearity Cu_{67} NC is successfully synthesized, and Cu_{67} possesses a hierarchical metal core structure of $Cu_5@Cu_{26}@Cu_{36}$. Despite the Cu core is intrinsically chiral, the whole cluster is a racemate. When used as catalyst for eCO_2RR, Cu_{67} exhibits high selectivity toward C_{2+} products, evidenced by a 39.52% FE_{C2H4} at -0.8 V vs. RHE, and a 56.32% FE for the total C_{2+} products at -0.9 V vs. RHE. *In-situ* ATR-SEIRAS analysis reveals the general reaction pathway, where the key intermediate *COCHO for yielding the C_{2+} products is identified. DFT calculations further elucidates the reaction mechanism, where the rate-determining step is unraveled. This study not only highlights the great advantages of employing high-nuclearity Cu superatomic cluster as model and effective electrocatalysts, but also provides atomical-level mechanistic understanding for designing Cu nanocatalysts to achieve highly valuable products in eCO_2RR and other electrochemical reactions.

Acknowledgements

L. W. is grateful for the financial support from the National Natural Science Foundation of China (No. 21805170). Q. T. thanks the grants from the National Natural Science Foundation of China (No. 22473017) and the Chongqing Science and Technology Commission (CSTB2024NSCQ-MSX0250). Z. T. acknowledges the financial support from the Guangdong Natural Science Funds (No. 2023A0505050107).

Electronic Supplementary Material: Supplementary material (Experimental details, auxiliary diagrams, X-ray single-crystal diffraction parameters, additional eCO_2RR measurements, ATR-SEIRAS results, computational details, and additional computational results) is available in the online version of this article at https://doi.org/10.26599/NR.2025.94908144.

References

[1] Sullivan, I.; Goryachev, A.; Digdaya, I. A.; Li, X.; Atwater, H. A.; Vermaas, D. A.; Xiang, C. Coupling Electrochemical CO_2 Conversion with CO_2 Capture. *Nat. Catal.* **2021**, *4*, 952–958.

[2] Li, M.; Wang, H.; Luo, W.; Sherrell, P. C.; Chen, J.; Yang, J. Heterogeneous Single-Atom Catalysts for Electrochemical CO_2 Reduction Reaction. *Adv. Mater.* **2020**, *32*, 2001848.

[3] Tan, Y.; Sun, G.; Jiang, T.; Liu, D.; Li, Q.; Yang, S.; Chai, J.; Gao, S.; Yu, H.; Zhu, M. Symmetry Breaking Enhancing the Activity of Electrocatalytic CO_2 Reduction on an Icosahedron-Kernel Cluster by Cu Atoms Regulation. *Angew. Chem. Int. Ed.* **2024**, *63*, e202317471.

[4] Xu, G.; Peng, X.; Wu, C.; Xi, S.; Xiang, H.; Feng, L.; Liu, Z.; Duan, Y.; Gan, L.; Chen, S.; Kong, Y.; Ma, Y.; Nie, F.; Zhao, J.; Hai, X.; Wei, W.; Zhou, M.; Wang, T.; Yao, C.; Zhou, W.; Yan, H. Atomically Precise Ni Clusters Inducing Active NiN_2 Sites with Uniform-Large Vacancies towards Efficient CO_2-to-CO Conversion. *Nat. Commun.* **2025**, *16*, 3774.

[5] Wang, Z.; Chen, Z.; Du, X.; Zhang, Y.; Liu, Z.; Zang, S.-Q. Modulating the Electronic Properties of Single Ni Atom Catalyst via First-Shell Coordination Engineering to Boost Electrocatalytic Flue Gas CO_2 Reduction. *Adv. Funct. Mater.* **2025**, *35*, 2420994.

[6] Chen, Y.; Hu, F.; Hao, Y.; Wang, Y.; Xie, Y.; Wang, H.; Yin, L.; Yu, D.; Yang, H.; Ma, J.; Kai, D.; Li, L.; Peng,

S. In Situ Construction of Thiol-Silver Interface for Selectively Electrocatalytic CO_2 Reduction. *Nano Res.* **2022**, *15*, 3283–3289.

[7] Raciti, D.; Wang, C. Recent Advances in CO_2 Reduction Electrocatalysis on Copper. *ACS Energy Lett.* **2018**, *3*, 1545–1556.

[8] Albero, J.; Peng, Y.; García, H. Photocatalytic CO_2 Reduction to C2+ Products. *ACS Catal.* **2020**, *10*, 5734–5749.

[9] Choi, W.; Chae, Y.; Liu, E.; Kim, D.; Drisdell, W. S.; Oh, H.; Koh, J. H.; Lee, D. K.; Lee, U.; Won, D. H. Exploring the Influence of Cell Configurations on Cu Catalyst Reconstruction during CO_2 Electroreduction. *Nat. Commun.* **2024**, *15*, 8345.

[10] Yang, Y.; Zhang, L.-J.; Wang, X.-L.; Wang, R.; Zhao, Y.-X.; He, S.-G.; Zang, S.-Q. Consecutive C–C Coupling of CH_4 and CO_2 Mediated by Heteronuclear Metal Cations $CuTa^+$. *J. Am. Chem. Soc.* **2025**, *147*, 362–371.

[11] Yang, T.; Kuang, M.; Yang, J. Tandem Engineering for CO_2 Electrolysis toward Multicarbon Products. *Nano Res.* **2023**, *16*, 8670–8683.

[12] Nitopi, S.; Bertheussen, E.; Scott, S. B.; Liu, X.; Engstfeld, A. K.; Horch, S.; Seger, B.; Stephens, I. E. L.; Chan, K.; Hahn, C.; Nørskov, J. K.; Jaramillo, T. F.; Chorkendorff, I. Progress and Perspectives of Electrochemical CO_2 Reduction on Copper in Aqueous Electrolyte. *Chem. Rev.* **2019**, *119*, 7610–7672.

[13] Lum, Y.; Ager, J. W. Sequential Catalysis Controls Selectivity in Electrochemical CO_2 Reduction on Cu. *Energy Environ. Sci.* **2018**, *11*, 2935–2944.

[14] Liu, Y.; Tang, H.; Zhou, Y.; Lin, B.-L. Improved Catalytic Performance of CO_2 Electrochemical Reduction Reaction towards Ethanol on Chlorine-Modified Cu-Based Electrocatalyst. *Nano Res.* **2024**, *17*, 3761–3768.

[15] Liu, S.; Zhang, B.; Zhang, L.; Sun, J. Rational Design Strategies of Cu-Based Electrocatalysts for CO_2 Electroreduction to C_2 Products. *J. Energy Chem.* **2022**, *71*, 63–82.

[16] Dong, X.-Y.; Chen, H.; Wang, S.; Zou, R.-Y.; Zang, S.-Q.; Cai, J. Introducing La into a Customized Dual Cu Covalent Organic Framework to Steer CO_2 Electroreduction Selectivity from C_2H_4 to CH_4. *Adv. Mater.* **2025**, *37*, 2413710.

[17] Yang, R.; Duan, J.; Dong, P.; Wen, Q.; Wu, M.; Liu, Y.; Liu, Y.; Li, H.; Zhai, T. In Situ Halogen-Ion Leaching Regulates Multiple Sites on Tandem Catalysts for Efficient CO_2 Electroreduction to C_{2+} Products. *Angew. Chem. Int. Ed.* **2022**, *61*, e202116706.

[18] Yuan, X.; Chen, S.; Cheng, D.; Li, L.; Zhu, W.; Zhong, D.; Zhao, Z.-J.; Li, J.; Wang, T.; Gong, J. Controllable Cu^0-Cu^+ Sites for Electrocatalytic Reduction of Carbon Dioxide. *Angew. Chem. Int. Ed.* **2021**, *60*, 15344–15347.

[19] Sun, J.; Wu, Q.; Yan, X.; Li, L.; Tang, X.; Gong, X.; Yan, B.; Xu, Q.; Guo, Q.; He, J.; Shen, H. Structure Distortion Endows Copper Nanoclusters with Surface-Active Uncoordinated Sites for Boosting Catalysis. *JACS Au* **2024**, *4*, 3427–3435.

[20] Qiao, W.-Z.; Wang, Y.-J.; Li, S.; Wang, R.; Wu, J.; Zang, S.-Q. Integrating Homogeneous and Heterogeneous Catalysis in a Copper Nanocluster with Lewis Acid–Base Sites for Chemical Conversion of CO_2 and Propargylamine. *CCS Chem.* **2024**, *6*, 2131–2141.

[21] Zheng, K.; Xie, J. Cluster Materials as Traceable Antibacterial Agents. *Acc. Mater. Res.* **2021**, *2*, 1104–1116.

[22] Qin, L.; Chen, Y.; Liu, Z.; Chen, M.; Tang, Q.; Tang, Z. Construction of Atomic-Scale Compressive Strain for Oxime Electrosynthesis. *J. Am. Chem. Soc.* **2025**, *147*, 18003–18016.

[23] Deng, G.; Yun, H.; Bootharaju, M. S.; Sun, F.; Lee, K.; Liu, X.; Yoo, S.; Tang, Q.; Hwang, Y. J.; Hyeon, T. Copper Doping Boosts Electrocatalytic CO_2 Reduction of Atomically Precise Gold Nanoclusters. *J. Am. Chem. Soc.* **2023**, *145*, 27407–27414.

[24] Wang, Y.-X.; Zhang, F.-Q.; Qi, Z.; Zhao, X.; Zhang, N.; Li, H.; Li, H.; Zhang, X.-M. Photochemical Synthesis of $Ag_{12}Cu_7$ Nanocluster with Cuprophilicity-Related Long-Lived Phosphorescence. *Aggregate* **2025**, *6*, e675.

[25] Liu, Z.; Tan, H.; Li, B.; Hu, Z.; Jiang, D.; Yao, Q.; Wang, L.; Xie, J. Ligand Effect on Switching the Rate-Determining Step of Water Oxidation in Atomically Precise Metal Nanoclusters. *Nat. Commun.* **2023**, *14*, 3374.

[26] Sun, J.; Liu, J.; Su, H.-F.; Li, S.; Tang, X.; Xie, Z.; Xu, Z.; Jiang, W.; Wei, J.; Gong, X.; He, A.; Wang, S.; Jiang, D.; Zheng, N.; Shen, H. Eight-Electron Copper-Hydride Nanoclusters: Synthesis, Structure,

Alloying Chemistry and Photoluminescence. *Chem. Sci.* **2025**, *16*, 6392–6401.

[27] Yao, Q.; Zhu, M.; Yang, Z.; Song, X.; Yuan, X.; Zhang, Z.; Hu, W.; Xie, J. Molecule-like Synthesis of Ligand-Protected Metal Nanoclusters. *Nat. Rev. Mater.* **2025**, *10*, 89–108.

[28] Li, S.; Nagarajan, A. V.; Du, X.; Li, Y.; Liu, Z.; Kauffman, D. R.; Mpourmpakis, G.; Jin, R. Dissecting Critical Factors for Electrochemical CO$_2$ Reduction on Atomically Precise Au Nanoclusters. *Angew. Chem. Int. Ed.* **2022**, *61*, e202211771.

[29] Xiao, Y.; Wu, Z.; Yao, Q.; Xie, J. Luminescent Metal Nanoclusters: Biosensing Strategies and Bioimaging Applications. *Aggregate* **2021**, *2*, 114–132.

[30] Deng, G.; Kim, J.; Bootharaju, M. S.; Sun, F.; Lee, K.; Tang, Q.; Hwang, Y. J.; Hyeon, T. Body-Centered-Cubic-Kernelled Ag$_{15}$Cu$_6$ Nanocluster with Alkynyl Protection: Synthesis, Total Structure, and CO$_2$ Electroreduction. *J. Am. Chem. Soc.* **2023**, *145*, 3401–3407.

[31] Lee, S.; Bootharaju, M. S.; Deng, G.; Malola, S.; Baek, W.; Häkkinen, H.; Zheng, N.; Hyeon, T. [Cu$_{32}$(PET)$_{24}$H$_8$Cl$_2$](PPh$_4$)$_2$: A Copper Hydride Nanocluster with a Bisquare Antiprismatic Core. *J. Am. Chem. Soc.* **2020**, *142*, 13974–13981.

[32] Liu, L.; Wang, Z.; Wang, Z.; Wang, R.; Zang, S.; Mak, T. C. W. Mediating CO$_2$ Electroreduction Activity and Selectivity over Atomically Precise Copper Clusters. *Angew. Chem. Int. Ed.* **2022**, *61*, e202205626.

[33] Wu, Q.; Si, D.; Sun, P.; Dong, Y.; Zheng, S.; Chen, Q.; Ye, S.; Sun, D.; Cao, R.; Huang, Y. Atomically Precise Copper Nanoclusters for Highly Efficient Electroreduction of CO$_2$ towards Hydrocarbons via Breaking the Coordination Symmetry of Cu Site. *Angew. Chem. Int. Ed.* **2023**, *62*, e202306822.

[34] Li, J.-K.; Dong, J.-P.; Liu, S.-S.; Hua, Y.; Zhao, X.-L.; Li, Z.; Zhao, S.-N.; Zang, S.-Q.; Wang, R. Promoting CO$_2$ Electroreduction to Hydrocarbon Products via Sulfur-Enhanced Proton Feeding in Atomically Precise Thiolate-Protected Cu Clusters. *Angew. Chem. Int. Ed.* **2024**, *63*, e202412144.

[35] Mu, W.-L.; Li, L.; Cong, X.-Z.; Chen, X.; Xia, P.; Liu, Q.; Wang, L.; Yan, J.; Liu, C. Hierarchical Assembly of High-Nuclearity Copper(I) Alkynide Nanoclusters: Highly Effective CO$_2$ Electroreduction Catalyst toward Hydrocarbons. *J. Am. Chem. Soc.* **2024**, *146*, 28131–28140.

[36] Nguyen, T.-A. D.; Jones, Z. R.; Goldsmith, B. R.; Buratto, W. R.; Wu, G.; Scott, S. L.; Hayton, T. W. A Cu$_{25}$ Nanocluster with Partial Cu(0) Character. *J. Am. Chem. Soc.* **2015**, *137*, 13319–13324.

[37] Yuan, P.; Chen, R.; Zhang, X.; Chen, F.; Yan, J.; Sun, C.; Ou, D.; Peng, J.; Lin, S.; Tang, Z.; Teo, B. K.; Zheng, L.; Zheng, N. Ether‑Soluble Cu$_{53}$ Nanoclusters as an Effective Precursor of High‑Quality CuI Films for Optoelectronic Applications. *Angew. Chem. Int. Ed.* **2019**, *58*, 835–839.

[38] Duan, G.-Y.; Li, X.-Q.; Ding, G.-R.; Han, L.-J.; Xu, B.-H.; Zhang, S.-J. Highly Efficient Electrocatalytic CO$_2$ Reduction to C$_{2+}$ Products on a Poly(Ionic Liquid)-Based Cu^0–Cu^I Tandem Catalyst. *Angew. Chem. Int. Ed.* **2022**, *61*, e202110657.

[39] Dai, L.; Qin, Q.; Wang, P.; Zhao, X.; Hu, C.; Liu, P.; Qin, R.; Chen, M.; Ou, D.; Xu, C.; Mo, S.; Wu, B.; Fu, G.; Zhang, P.; Zheng, N. Ultrastable Atomic Copper Nanosheets for Selective Electrochemical Reduction of Carbon Dioxide. *Sci. Adv.* **2017**, *3*, e1701069.

[40] Pillay, M. N.; Zyl, W. E. van; Liu, C. W. A Construction Guide for High-Nuclearity (≥50 Metal Atoms) Coinage Metal Clusters at the Nanoscale: Bridging Molecular Precise Constructs with the Bulk Material Phase. *Nanoscale* **2020**, *12*, 24331–24348.

[41] Chen, Q.; Ke, Q.; Zhao, X.; Feng, Y.; Zhao, Q.; Feng, J.; Ge, X.; Chen, X. Transition Metal Doped into Defective Boron Nitride Nanotubes for CO$_2$RR: Regulation of Catalytic Activity and Mechanism by Curvature Effect. *Sep. Purif. Technol.* **2024**, *338*, 126552.

[42] Lv, K.; Wan, D.; Pan, R.; Suo, W.; Zhu, Y. Curvature of NCNTs Induced Selectivity of CO$_2$ Electroreduction into CO. *Carbon Neutralization* **2022**, *1*, 189–197.

[43] Sagadevan, A.; Ghosh, A.; Maity, P.; Mohammed, O. F.; Bakr, O. M.; Rueping, M. Visible-Light Copper Nanocluster Catalysis for the C–N Coupling of Aryl Chlorides at Room Temperature. *J. Am. Chem. Soc.* **2022**, *144*, 12052–12061.

[44] Yan, B.; Sun, J.; Liu, J.; Li, L.; Deng, H.; Xu, Q.; Wang, S.; Shen, H. Flat-Shaped Copper Nanoclusters with Near-Infrared Absorption for Enhanced Photothermal Conversion. *JACS Au* **2025**, *5*,

1884–1893.

[45] Dong, C.; Huang, R.; Sagadevan, A.; Yuan, P.; Gutiérrez‐Arzaluz, L.; Ghosh, A.; Nematulloev, S.; Alamer, B.; Mohammed, O. F.; Hussain, I.; Rueping, M.; Bakr, O. M. Isostructural Nanocluster Manipulation Reveals Pivotal Role of One Surface Atom in Click Chemistry. *Angew. Chem. Int. Ed.* **2023**, *62*, e202307140.

[46] Qin, H.-N.; He, M.-W.; Wang, J.; Li, H.-Y.; Wang, Z.-Y.; Zang, S.-Q.; Mak, T. C. W. Thiacalix[4]Arene Etching of an Anisotropic $Cu_{70}H_{22}$ Intermediate for Accessing Robust Modularly Assembled Copper Nanoclusters. *J. Am. Chem. Soc.* **2024**, *146*, 3545–3552.

[47] Sun, X.; Wang, Y.; Wu, Q.; Han, Y.; Gong, X.; Tang, X.; Aikens, C. M.; Shen, H.; Zheng, N. Cu_{66} Nanoclusters from Hierarchical Square Motifs: Synthesis, Assembly, and Catalysis. *Aggregate* **2024**, *6*, e651.

[48] Han, B.-L.; Alkan, F.; Yuan, Z.-R.; Mahato, P.; Wang, Z.; Tung, C.-H.; Sun, D. Hydrogen-Bonding-Assisted Assembly of Stable High-Nuclearity Copper(I)-Alkyne Nanoclusters for X-Ray Scintillation. *Angew. Chem. Int. Ed. n/a*, e202507412.

[49] Liu, S.; Yin, S.; Wang, Z.; Xu, Y.; Li, X.; Wang, L.; Wang, H. AuCu Nanofibers for Electrosynthesis of Urea from Carbon Dioxide and Nitrite. *Cell Rep. Phy. Sci.* **2022**, *3*, 100869.

[50] Guo, T.; Yun, Y.; Li, T.; Xia, J.; Zhou, J.; Sheng, H.; Zhu, M. Double Reactive Oxygen Species System Photoinduced by Cu_8 NCs: Synergistic Catalysis of Phenylacetylene Self-Coupling Reaction. *Nanoscale* **2025**, *17*, 4670–4675.

[51] Ravel, B.; Newville, M. ATHENA, ARTEMIS, HEPHAESTUS: Data Analysis for X-Ray Absorption Spectroscopy Using IFEFFIT. *J Synchrotron Rad* **2005**, *12*, 537–541.

[52] Jia, T.; Guan, Z.-J.; Zhang, C.; Zhu, X.-Z.; Chen, Y.-X.; Zhang, Q.; Yang, Y.; Sun, D. Eight-Electron Superatomic Cu_{31} Nanocluster with Chiral Kernel and NIR-II Emission. *J. Am. Chem. Soc.* **2023**, *145*, 10355–10363.

[53] Jadzinsky, P. D.; Calero, G.; Ackerson, C. J.; Bushnell, D. A.; Kornberg, R. D. Structure of a Thiol Monolayer-Protected Gold Nanoparticle at 1.1 Å Resolution. *Science* **2007**, *318*, 430–433.

[54] Deng, G.; Lee, K.; Deng, H.; Malola, S.; Bootharaju, M. S.; Häkkinen, H.; Zheng, N.; Hyeon, T. Alkynyl-Protected Chiral Bimetallic $Ag_{22}Cu_7$ Superatom with Multiple Chirality Origins. *Angew. Chem. Int. Ed.* **2023**, *135*, e202217483.

[55] Wan, X.-K.; Cheng, X.-L.; Tang, Q.; Han, Y.-Z.; Hu, G.; Jiang, D.; Wang, Q.-M. Atomically Precise Bimetallic $Au_{19}Cu_{30}$ Nanocluster with an Icosidodecahedral Cu_{30} Shell and an Alkynyl–Cu Interface. *J. Am. Chem. Soc.* **2017**, *139*, 9451–9454.

[56] Cook, A. W.; Jones, Z. R.; Wu, G.; Scott, S. L.; Hayton, T. W. An Organometallic Cu_{20} Nanocluster: Synthesis, Characterization, Immobilization on Silica, and "Click" Chemistry. *J. Am. Chem. Soc.* **2018**, *140*, 394–400.

[57] Lei, Z.; Wan, X.-K.; Yuan, S.-F.; Guan, Z.-J.; Wang, Q.-M. Alkynyl Approach toward the Protection of Metal Nanoclusters. *Acc. Chem. Res.* **2018**, *51*, 2465–2474.

[58] Li, S.; Yan, X.; Tang, J.; Cao, D.; Sun, X.; Tian, G.; Tang, X.; Guo, H.; Wu, Q.; Sun, J.; He, J.; Shen, H. Cu_{26} Nanoclusters with Quintuple Ligand Shells for CO_2 Electrocatalytic Reduction. *Chem. Mater.* **2023**, *35*, 6123–6132.

[59] Shingyouchi, Y.; Ogami, M.; Biswas, S.; Tanaka, T.; Kamiyama, M.; Ikeda, K.; Hossain, S.; Yoshigoe, Y.; Osborn, D. J.; Metha, G. F.; Kawawaki, T.; Negishi, Y. Ligand-Dependent Intracluster Interactions in Electrochemical CO_2 Reduction Using Cu_{14} Nanoclusters. *Small* **2025**, *21*, 2409910.

[60] Zhang, L.; Feng, J.; Liu, S.; Tan, X.; Wu, L.; Jia, S.; Xu, L.; Ma, X.; Song, X.; Ma, J.; Sun, X.; Han, B. Atomically Dispersed Ni–Cu Catalysts for pH-Universal CO_2 Electroreduction. *Adv. Mater.* **2023**, *35*, 2209590.

[61] Wei, S.; Xu, Y.; Song, T.; Dai, H.; Li, F.; Gao, X.; Zhai, Y.; Gong, S.; Li, R.; Zhang, X.; Chan, K. Steering the Absorption Configuration of Intermediates over Pd-Based Electrocatalysts toward Efficient and Stable CO_2 Reduction. *J. Am. Chem. Soc.* **2025**, *147*, 4219–4229.

[62] Ma, H.; Ibáñez-Alé, E.; You, F.; López, N.; Yeo, B. S. Electrochemical Formation of C_{2+} Products Steered by Bridge-Bonded *CO Confined by *OH Domains. *J. Am. Chem. Soc.* **2024**, *146*, 30183–30193.

[63] Firet, N. J.; Smith, W. A. Probing the Reaction

Mechanism of CO_2 Electroreduction over Ag Films via Operando Infrared Spectroscopy. *ACS Catal.* **2017**, *7*, 606–612.

[64] Delmo, E. P.; Wang, Y.; Song, Y.; Zhu, S.; Zhang, H.; Xu, H.; Li, T.; Jang, J.; Kwon, Y.; Wang, Y.; Shao, M. In Situ Infrared Spectroscopic Evidence of Enhanced Electrochemical CO_2 Reduction and C–C Coupling on Oxide-Derived Copper. *J. Am. Chem. Soc.* **2024**, *146*, 1935–1945.

[65] Liu, S.; Yin, Y.; Yang, J.; Zhao, W.; Zhou, M.; Qin, H.; Jiao, J.; Wang, Y.; Wang, H.; Tong, X.; Xu, Y.; Sun, X.; Zhu, Q.; Fan, M.; Kang, X.; Han, B. Temperature-Dependent Pathways in Carbon Dioxide Electroreduction. *Sci. Bull.* **2025**, *70*, 889–896.

[66] Ma, F.; Zhang, P.; Zheng, X.; Chen, L.; Li, Y.; Zhuang, Z.; Fan, Y.; Jiang, P.; Zhao, H.; Zhang, J.; Dong, Y.; Zhu, Y.; Wang, D.; Wang, Y. Steering the Site Distance of Atomic Cu−Cu Pairs by First-Shell Halogen Coordination Boosts CO_2-to-C_2 Selectivity. *Angew. Chem. Int. Ed.* **2024**, *63*, e202412785.

[67] Bell, A. T.; Head-Gordon, M. Mechanism of CO_2 Reduction at Copper Surfaces: Pathways to C_2 Products. *ACS Catal.* **2018**, *8*, 1490–1499.

[68] Zhang, Q.; Tsai, H. J.; Li, F.; Wei, Z.; He, Q.; Ding, J.; Liu, Y.; Lin, Z.-Y.; Yang, X.; Chen, Z.; Hu, F.; Yang, X.; Tang, Q.; Yang, H. B.; Hung, S.-F.; Zhai, Y. Boosting the Proton-Coupled Electron Transfer via Fe−P Atomic Pair for Enhanced Electrochemical CO_2 Reduction. *Angew. Chem. Int. Ed.* **2023**, *62*, e202311550.

Electronic Supplementary Material

Alkynyl-protected Cu_{67} nanocluster superatom: Structure anatomy and electrochemical CO_2 reducion study

Ziyi Liu[1,§], Siqi Li[2,§], Lancheng Zhao[3,§], Lubing Qin[1], Jingwen Yang[1], Tao Wu[1], Likai Wang[3] (✉), Qing Tang[2] (✉), and Zhenghua Tang[1] (✉)

[1] *New Energy Research Institute, School of Environment and Energy, South China University of Technology, Guangzhou Higher Education Mega Centre, Guangzhou 510006, China*
[2] *School of Chemistry and Chemical Engineering, Chongqing Key Laboratory of Theoretical and Computational Chemistry, Chongqing University, Chongqing 401331, China*
[3] *School of Chemistry and Chemical Engineering, Shandong University of Technology, Zibo 255049, China*
[§] *Ziyi Liu, Siqi Li, and Lancheng Zhao contributed equally to this work.*

Supporting information to https://doi.org/10.26599/NR.2025.94908145

Experimental Section

Materials and chemicals： Dichloromethane (DCM), *n*-hexane and toluene were purchased from Zhiyuan Chemical Reagents (Tianjin, China). Cuprous acetate (Cu(OAc)), phenylacetylene (HC≡CPh), diphenylsilane (Ph_2SiH_2), XC-72 was purchased from Energy Chemical (Shanghai, China). Deionized water with a resistivity of 18.3 MΩ cm^{-1} was obtained using a Barnstead Nanopure water system. All chemicals were used as received without further treatment.

Physical measurements and instrumentation： The surface chemical compositions and valence states were examined by X-ray photoelectron spectroscopy (XPS, Phi X-tool instrument). UV-vis absorption spectra of the clusters were recorded by a Shimadzu 2600 spectrophotometer (Japan). *In-situ* attenuated total reflection surface enhanced infrared spectroscopy (ATR-SEIRAS) measurements were performed on a Nicolet 6700 FTIR spectrometer with silicon as the prismatic window. The single crystal data collection for $[Cu_{67}(C{\equiv}CPh)_{24}(OAc)_{18}]^-$ (Cu_{67}) was performed on an Agilent Technologies Super Nova single-crystal diffractometer using Mo Kα (λ = 0.71073 Å). In the Olex 2 graphical interface, SHELXT was used to solve and refine the structure. All non-hydrogen atoms were first refined isotropically then anisotropically. All of the hydrogen atoms of the ligand are placed at computational positions with fixed isotropic thermal parameters and are included in the final stage of the calculation of the structure factors for the full matrix least squares refinement. ^1H NMR spectrum was recorded on a Bruker Ascend 400 M Hz. XAFS measurements were performed at the BL14W1 beamline of the Shanghai Synchrotron Radiation Facility (SSRF) using a Si (311) crystal monochromator. Prior to beamline analysis, samples were pressed into thin sheets with a diameter of 1 cm and sealed with Kapton tape. EXAFS spectrum at the Cu K-edge were recorded in transmission mode.

Synthesis of $[Cu_{67}(C{\equiv}CPh)_{24}(OAc)_{18}]^-$ nanocluster: A pale green suspension of Cu(OAc) (111 mg, 0.9 mmol) in dichloromethane (DCM, 10 mL) was stirred vigorously at room temperature. Phenylacetylene (PhC≡CH, 64 µL, 0.6 mmol) was added via a micropipette, leading to the immediate precipitation of a bright yellow powder, indicative of the formation of $[Cu(C{\equiv}CPh)]_n$. A DCM solution (2 mL) of diphenylsilane (Ph_2SiH_2, 100 µL, 0.54 mmol) was slowly added dropwise to this suspension. The reaction mixture was stirred for 9 h, during which the color transitioned to a dark brown. After centrifugation (8000 rpm, 1 min) to remove insoluble residues, the supernatant was concentrated by rotary evaporation and dried under vacuum. The crude product was washed with hexane and a minimal amount of ethyl acetate to remove unreacted ligands. The resulting solid was dissolved in toluene and subjected to vapor diffusion with hexane as the antisolvent at 4°C for 7 days, yielding hexagonal black crystals (Figure S1) suitable for single-crystal X-ray diffraction analysis (Yield: ~15.4%，based on Cu). The CCDC number of $[Cu_{67}(C{\equiv}CPh)_{24}(OAc)_{18}]^-$ is 2417379.

Electrochemical measurements： All electrochemical measurements were performed in a three-compartment flow cell. The electrochemical reduction of CO_2 was carried out using a CHI 760 electrochemical workstation. The working electrode was carbon paper modified with Cu_{67} NCs, the reference electrode was Ag/AgCl and the counter electrode was Pt foil. A CO_2-saturated 1 M KOH solution was used as the electrolyte. During the electrochemical reduction tests, CO_2 gas was delivered at an average rate of 25 mL min^{-1} under ambient conditions and placed directly into the gas sampling loop of a gas chromatography (GC 9560). The gas chromatography was equipped with a thermal conductivity detector (TCD) for the detection of H_2, flame ionization detector (FID) for the detection of hydrocarbons, and methanation tower (Agilent) before FID for the detection of CO. Pure Ar was used as the carrier gas for all compartments of the GC. The liquid phase products were detected by ^1H NMR.

Electrochemical measurements： All electrochemical measurements were performed in a three-compartment flow cell. The electrochemical reduction of CO_2 was carried out using a CHI 760 electrochemical workstation. The working electrode was carbon paper modified with Cu_{67} NCs, the reference electrode was Ag/AgCl and the counter electrode was Pt foil. A CO_2-saturated 1 M KOH solution was used as the electrolyte. During the electrochemical reduction tests, CO_2 gas was delivered at an average rate of 25 mL min^{-1} under ambient conditions and placed directly into the gas sampling loop of a gas chromatography (GC 9560). The gas chromatography was

equipped with a thermal conductivity detector (TCD) for the detection of H_2, flame ionization detector (FID) for the detection of hydrocarbons, and methanation tower (Agilent) before FID for the detection of CO. Pure Ar was used as the carrier gas for all compartments of the GC. The liquid phase products were detected by ^{1}H NMR.

Electrochemical *in situ* ATR-SEIRAS measurements： The *in situ* ATR-SEIRAS tests were carried out on a Nicolet 6700 FTIR spectrometer equipped with an MCT (mercury-cadmium-tellurium) detector. The working electrode was a columnar silicon block with a gold film deposited on its surface by chemical deposition. Carbon rods and Ag/AgCl were used as counter electrode and reference electrode, respectively. Prior to the test, 5 mg of carbon black XC-72 was dispersed in 1 mL of ethanol and 20 μL of the dispersion was dropwise cast onto the gold film. Subsequently, 30 μL of the DCM solution containing Cu_{67} NCs and 20 μL of the Nafion solution dissolved in ethanol were added sequentially. After complete evaporation of the solvent, it was used as a working electrode for electrochemical tests.

Computational details： The density functional theory (DFT) calculations on the electrocatalytic activity were performed using the CP2K package (version 2023.1)[1]. To expedite the calculation convergence, we simplified the C≡C-Ph groups with C≡C-CH_3 groups. The nanoclusters were placed within a cubic (25 Å × 25Å × 25 Å), and the electronic structure calculations are described by DFT with spin-polarized Perdew−Burke−Ernzerhof (PBE) functional mixed double-ζ Gaussian and plane-wave (GPW) basis set, with an energy cutoff of 400 Ry[2]. The core electrons were modeled by Goedecker-Teter-Hutter (GTH) for the pseudopotentials of Cu, O, C and H, respectively. In addition, dispersion corrections were applied using the DFT-D3 method to account for van der Waals interactions[3,4].

According to the computational hydrogen electrode (CHE) model[5], the alteration in Gibbs free energy for each CO_2 reduction reaction (CO_2 RR) elementary reaction can be calculated as follows:

$$\Delta G=\Delta E+\Delta ZPE-T\Delta S$$

where ΔE, ΔZPE and ΔS are the change of the total energy that can be directly obtained from DFT calculations, the difference of zero-point energy, and the change of entropy at 298.15 K, respectively. For the adsorbed intermediates, only vibrational entropy is considered, which is calculated from the DFT calculated vibrational frequencies. In addition, due to the inaccurate description of CO_2 and CO molecules by PBE functional[2,6], we added correction of -0.34 eV for CO and +0.10 eV for CO_2[7].

Supplementary Figures

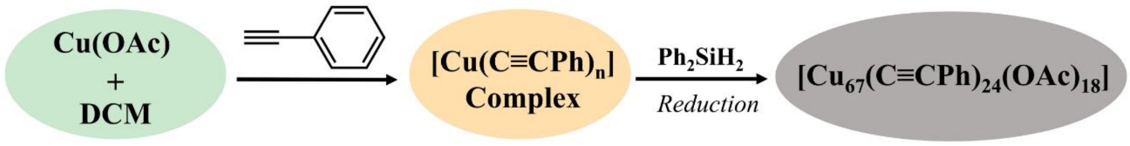

Scheme S1. The synthetic route for Cu_{67} nanoclusters.

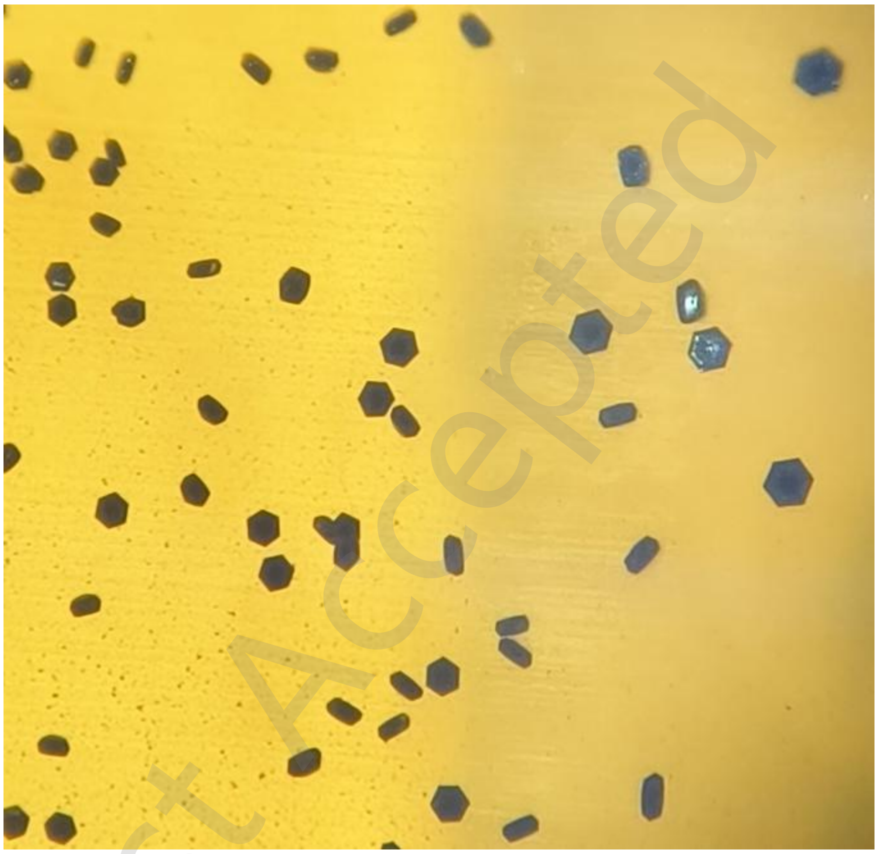

Figure S1. Photographs of single crystal of Cu_{67} clusters.

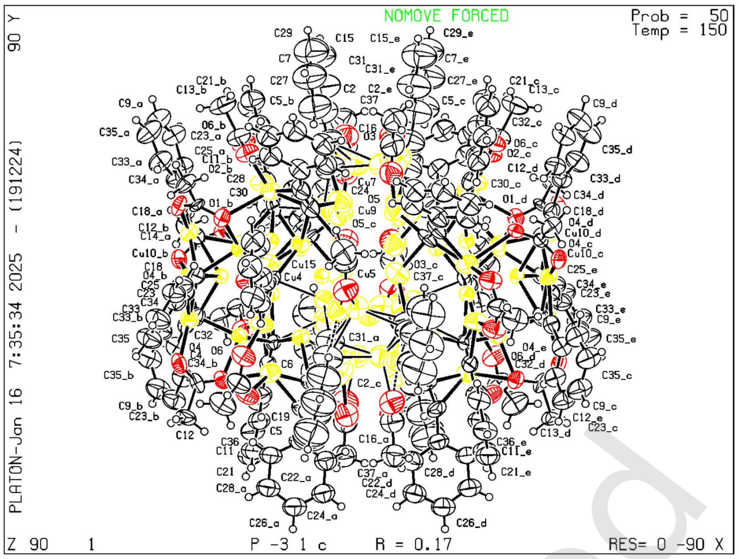

Figure S2. The thermal ellipsoids of the ORTEP diagram of Cu_{67}.

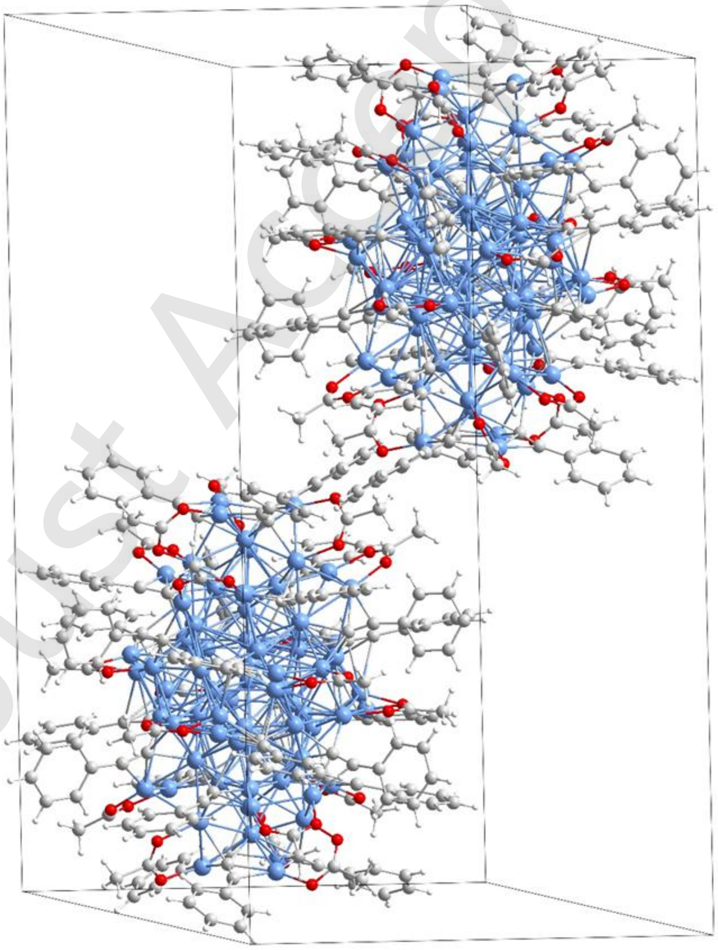

Figure S3. Packing of Cu_{67} clusters in a unit cell. Color legend: Cu, blue; O red; C, grey; H, white.

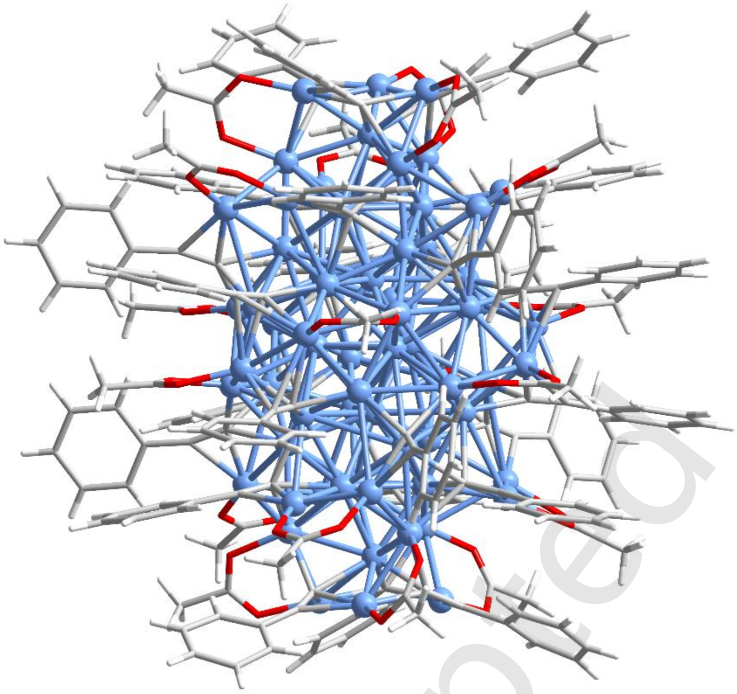

Figure S4. Side view of the overall structure of Cu_{67}. Color legend: Cu, blue; O red; C, grey; H, white.

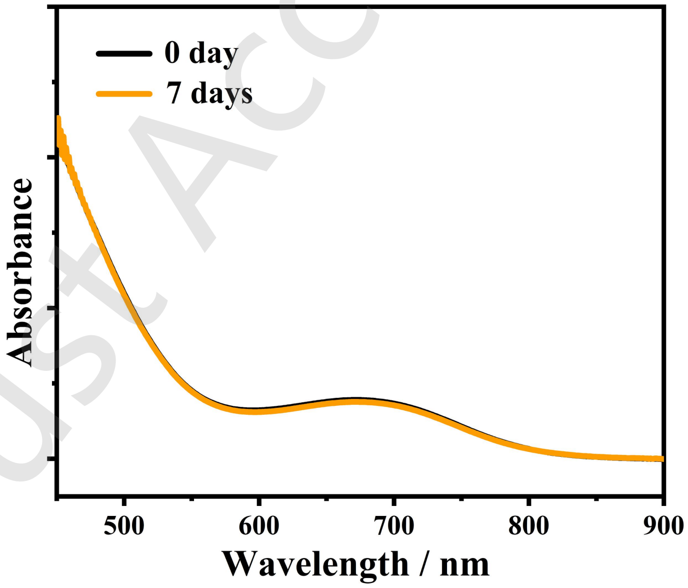

Figure S5. Comparison of Cu_{67} absorbance before and after one week.

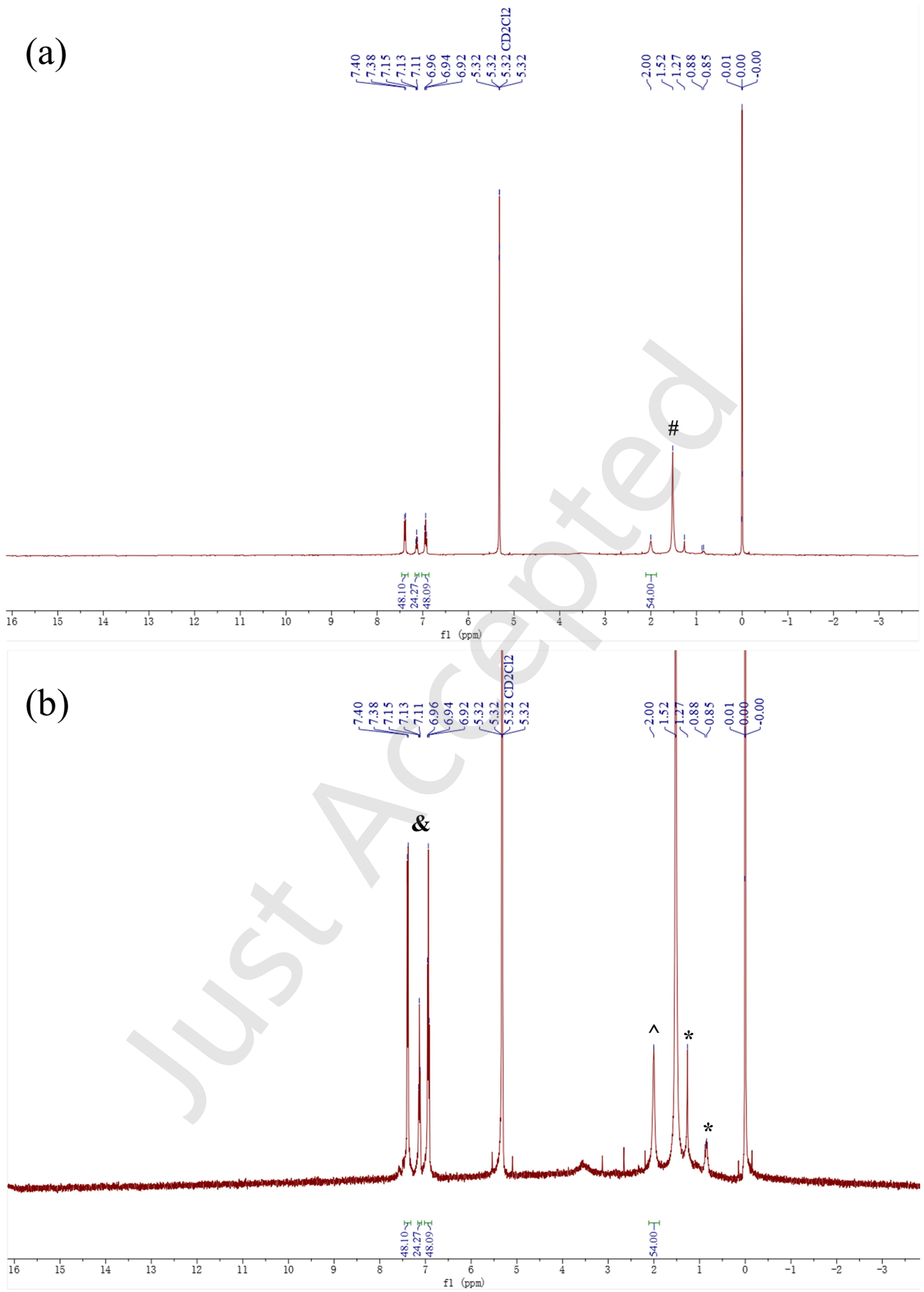

Figure S6. (a, b) ^{1}H NMR spectra of Cu_{67} in CD_2Cl_2. The marked peak in (a) corresponds to water (#); the marked peaks in (b) correspond to phenylacetylene (&), OAc (^), and *n*-hexane (*).

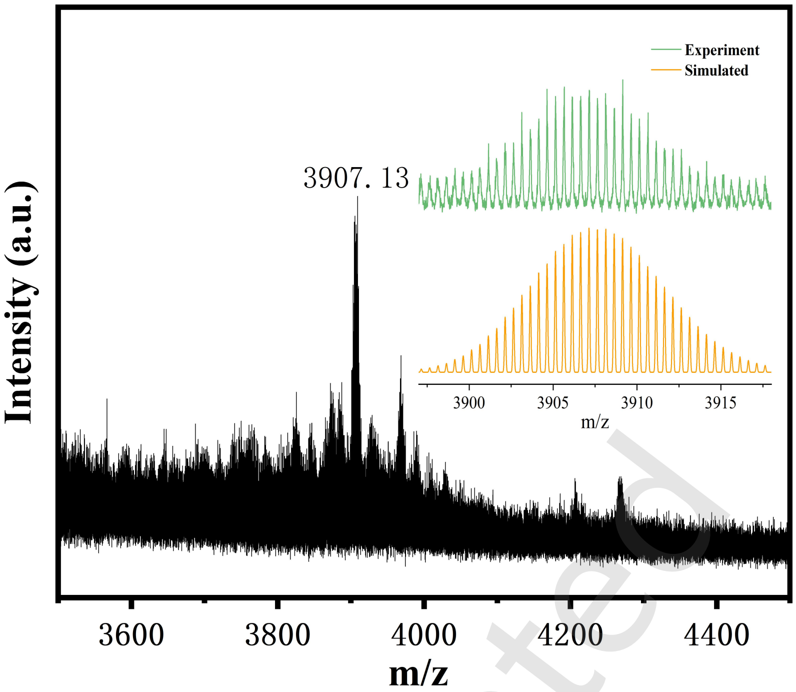

Figure S7. ESI-MS spectrum of Cu_{67} NC. The inset compares the experimental (green) and simulated (orange) isotopic patterns for the peak of $[Cu_{67}(C{\equiv}CPh)_{24}(OAc)_{17}+2Cu]^{2+}$. The molecular formula of Cu_{67} nanocluster is $[Cu_{67}(C{\equiv}CPh)_{24}(OAc)_{18}]^{-}$.

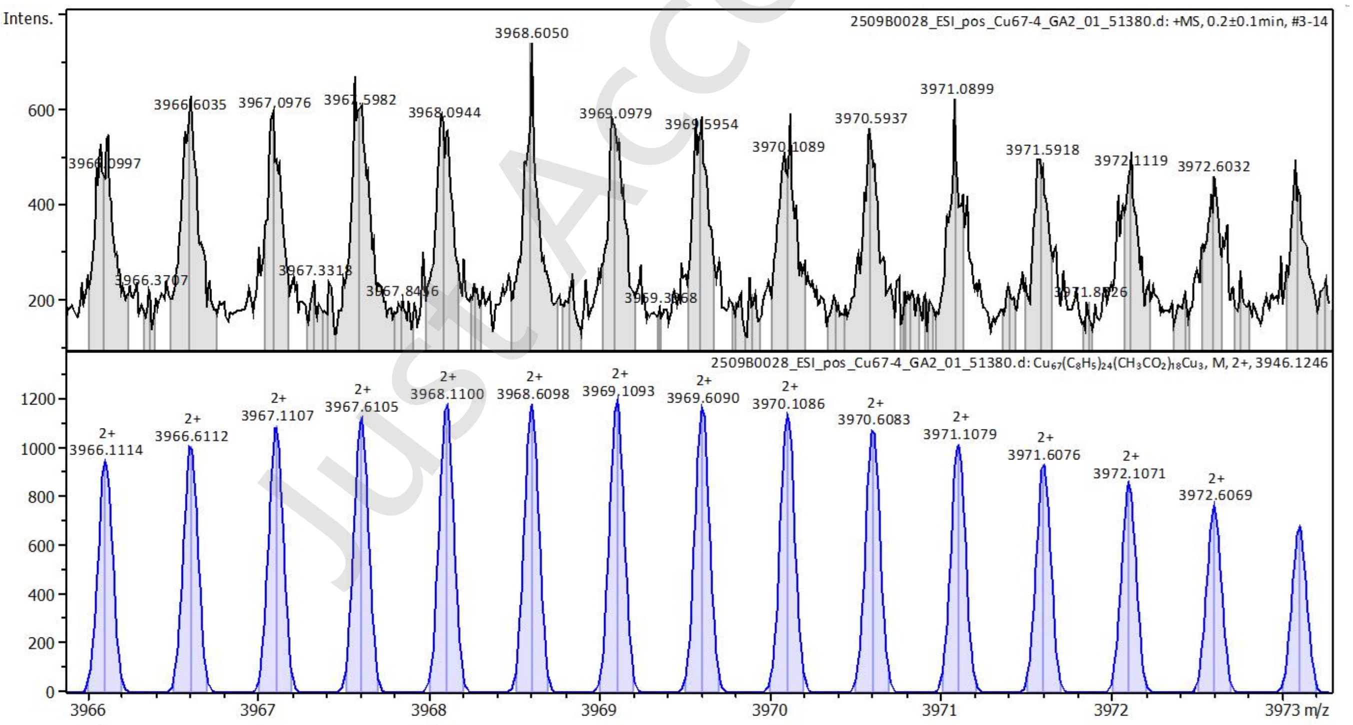

Figure S8. Partial ESI-MS of Cu_{67} NC. The experimental (top) and calculated peaks assignable to the $[Cu_{67}(C{\equiv}CPh)_{24}(OAc)_{18}+3Cu]^{2+}$.

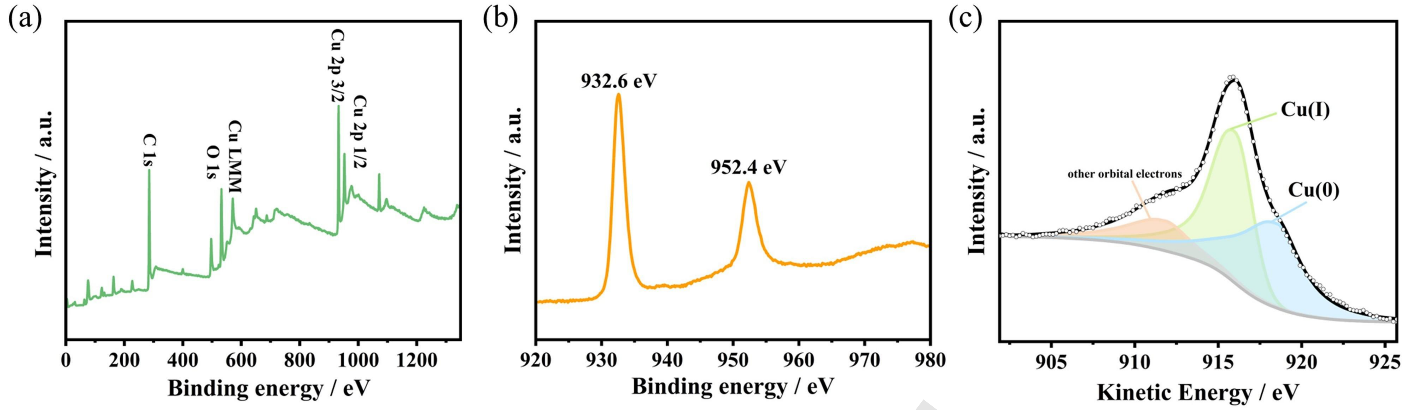

Figure S9. (a) The XPS spectrum of Cu_{67}; (b) The Cu 2p high-resolution XPS spectrum of Cu_{67}; (C) XPS Auger spectrum of Cu_{67}.

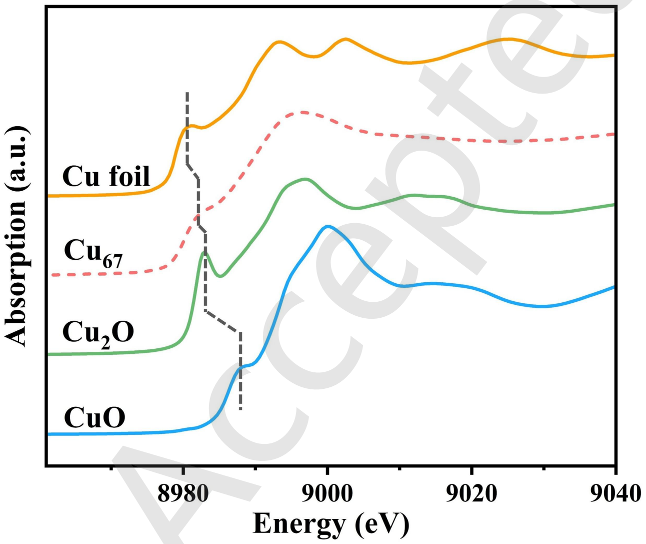

Figure S10. XANES spectrum of Cu_{67} and the reference samples.

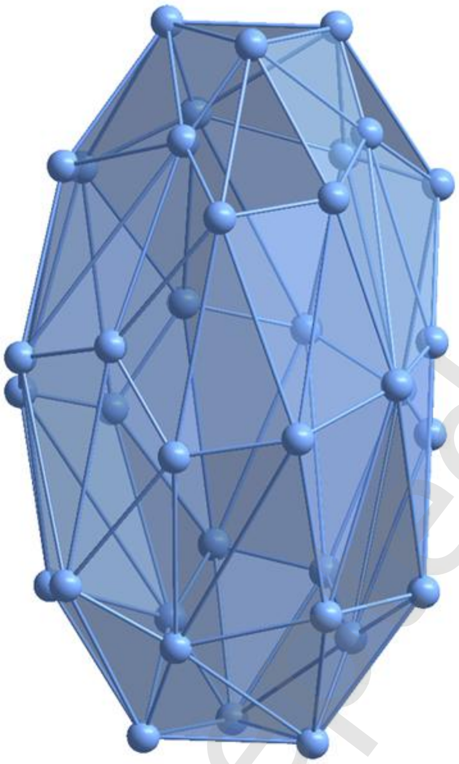

Figure S11. Connecting surfaces of the outer structure of Cu$_{67}$. Color labels: Cu: blue.

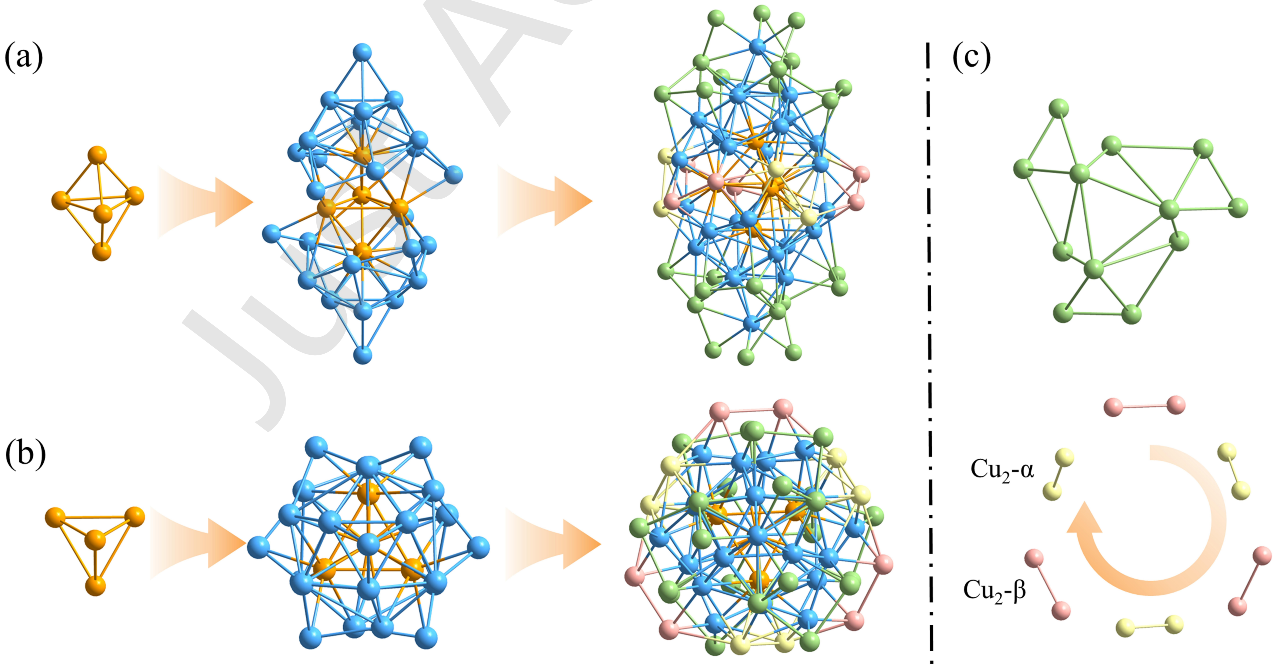

Figure S12. (a) Side and (bb) top views of the Cu$_{67}$ three-layer structural assembly; (c) Structural demonstration of a Cu$_{12}$ moiety and six Cu$_2$ units.

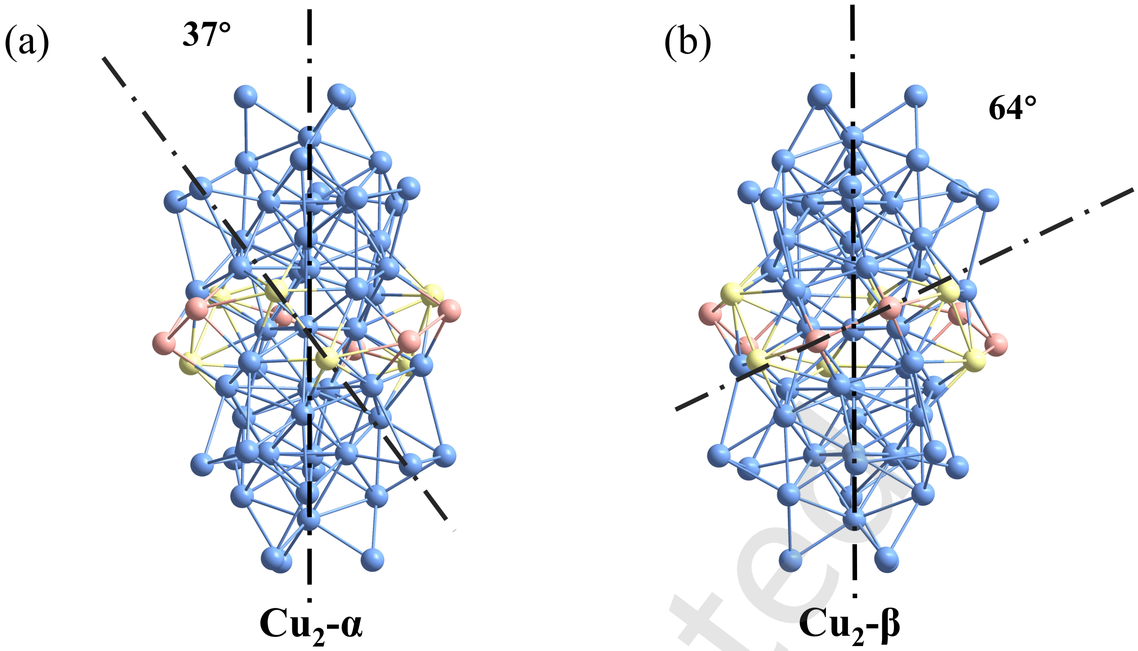

Figure S13. (a) Cu_2-α unit (yellow) connected to motif B with a torsion angle of ~37° with respect to the C_3 axis; (b) Cu_2-β unit (pink-orange) connected to motif D with a torsion angle of ~64° with respect to the C3 axis.

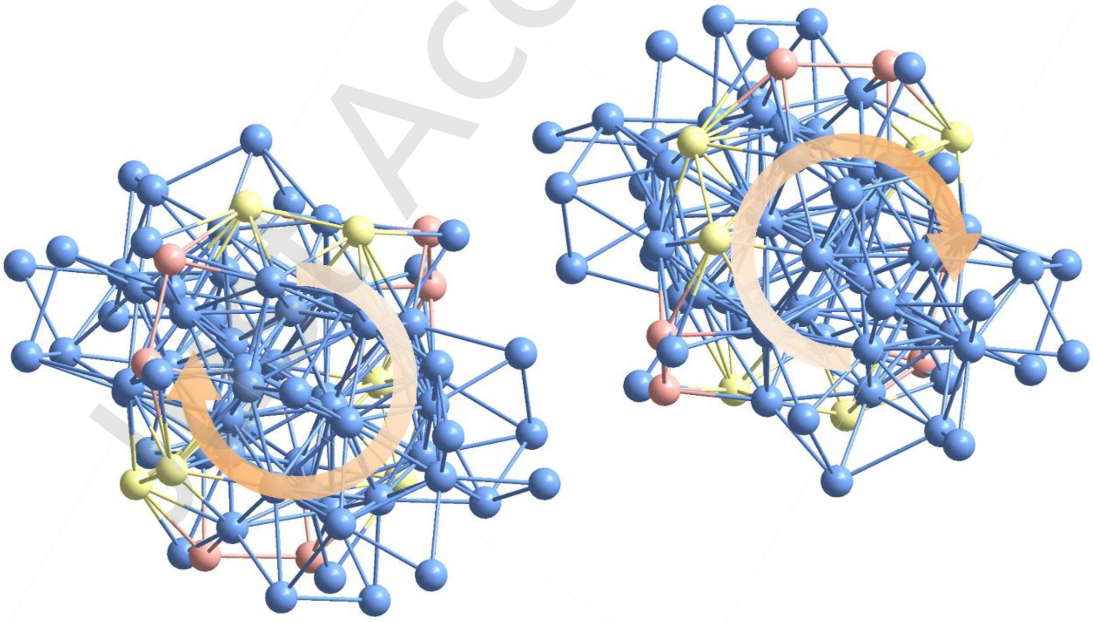

Figure S14. Two chiral enantiomers contained in a single crystal cell of Cu_{67}.

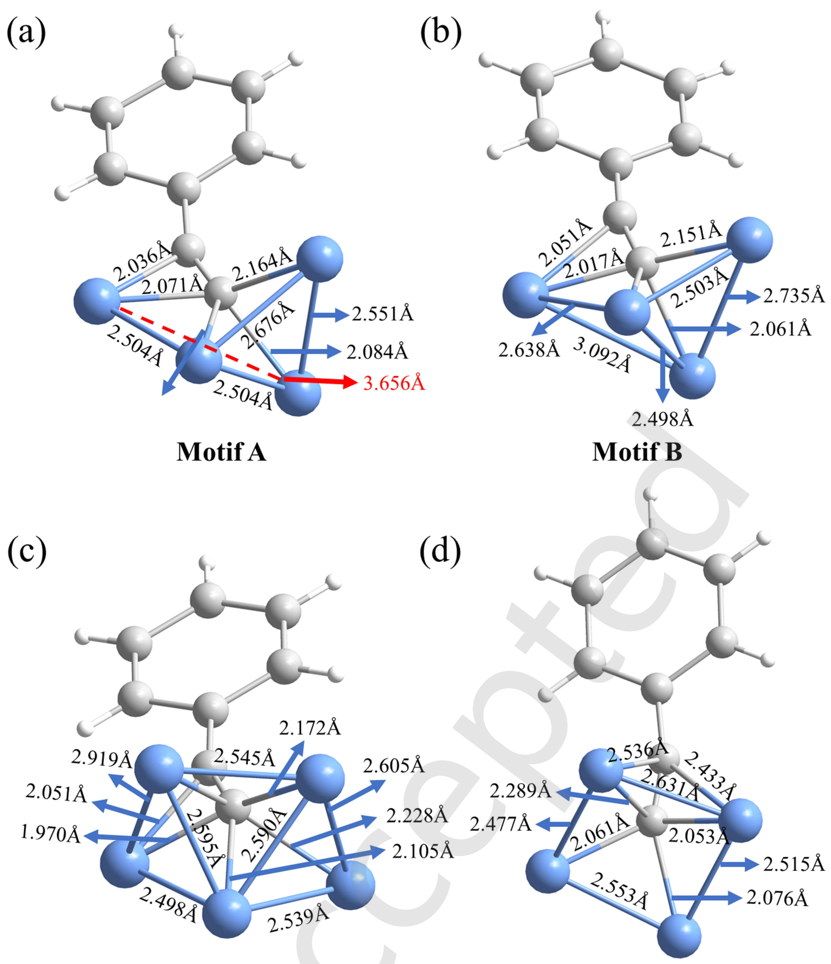

Motif A **Motif B** **Motif C** **Motif D**

Figure S15. Detailed bond length data for (a) Motif A, (b) Motif B, (c) Motif C and (d) Motif D. Color labels: Cu: blue; C: grey; H: white.

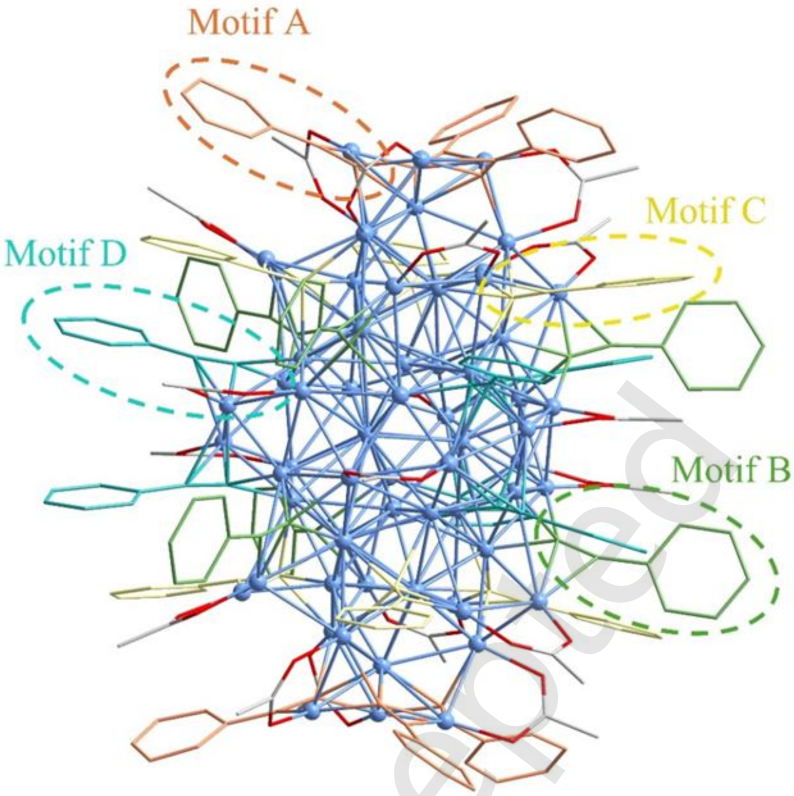

Figure S16. Distribution of motif A-D on Cu_{67}. Color labels: Cu: blue; O: red; C (Motif A): orange; C (Motif B): green; C (Motif C): yellow; C (Motif D): turquoise; C (Motif E): grey.

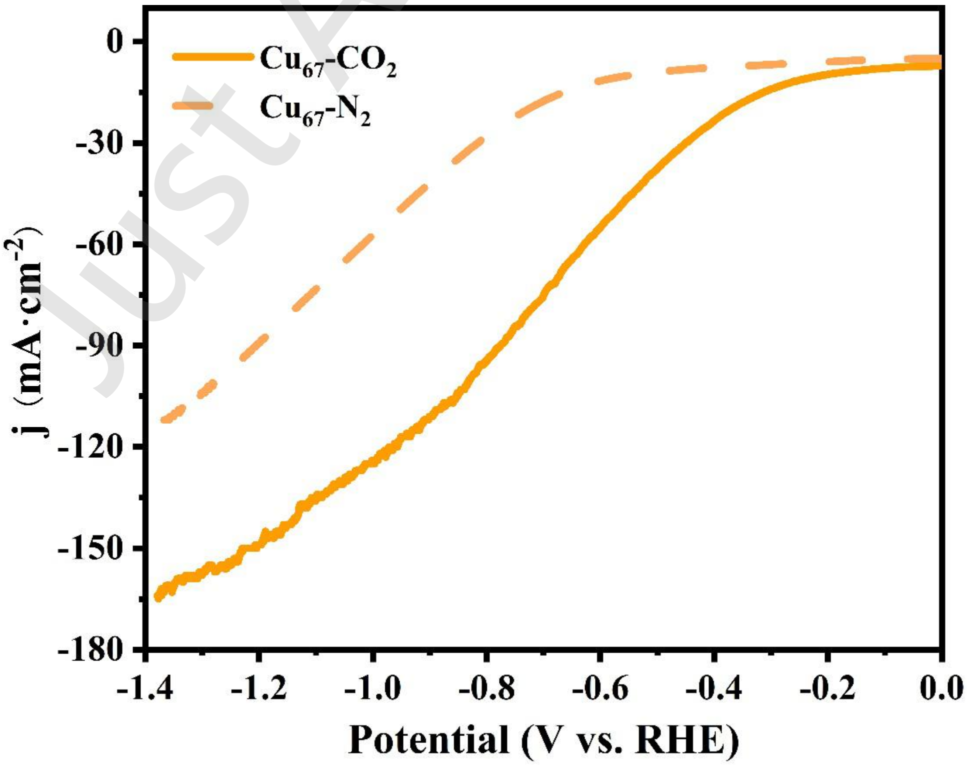

Figure S17. LSV curves of Cu_{67} in 1 M KOH saturated with CO_2 and N_2.

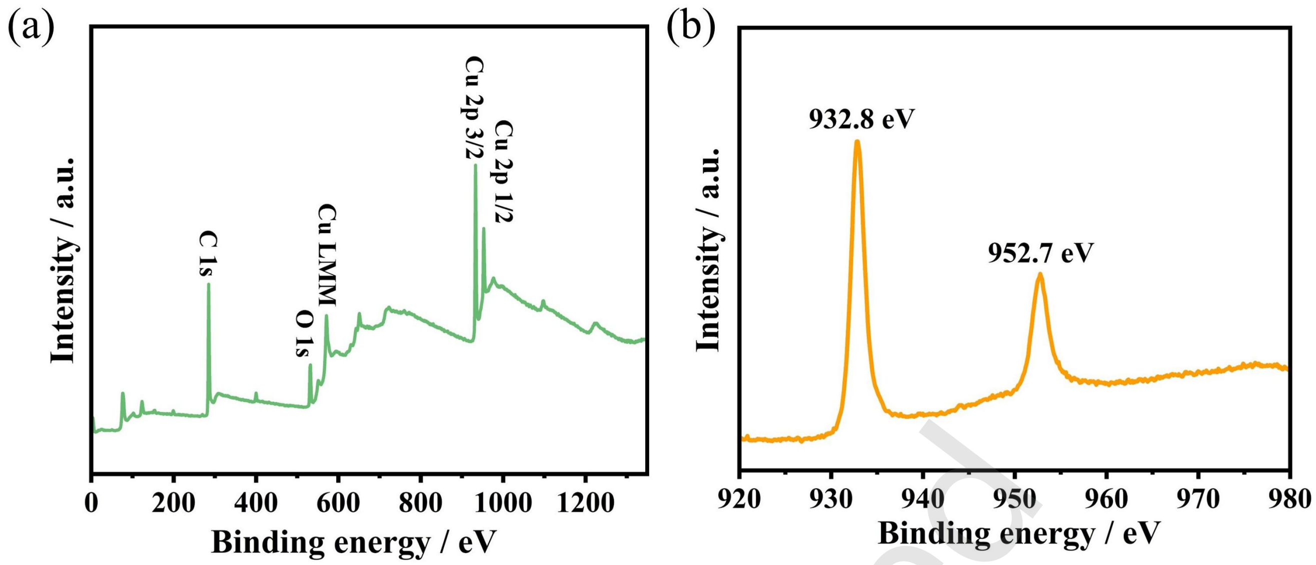

Figure S18. (a) XPS spectrum of Cu_{67} after eCO_2RR; (b) High-resolution Cu 2p XPS spectrum of Cu_{67} after eCO_2RR.

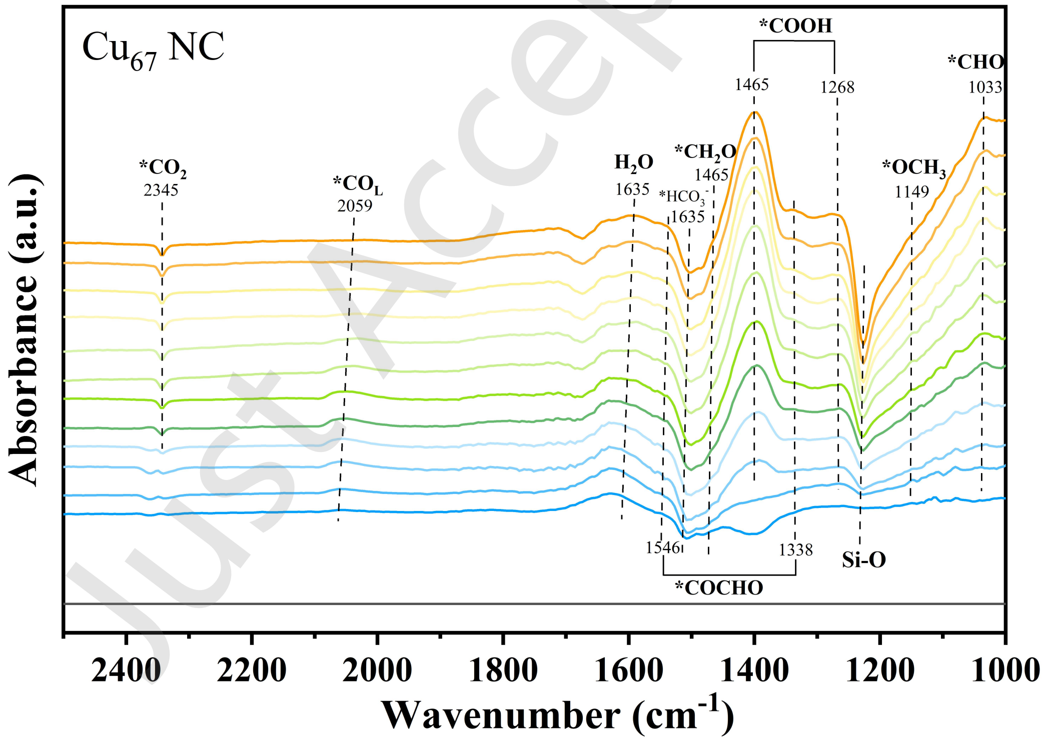

Figure S19. *In-situ* ATR-SEIRAS complete spectrum of Cu_{67} at applied potentials ranging from -0.4 to -1.2 V vs. RHE.

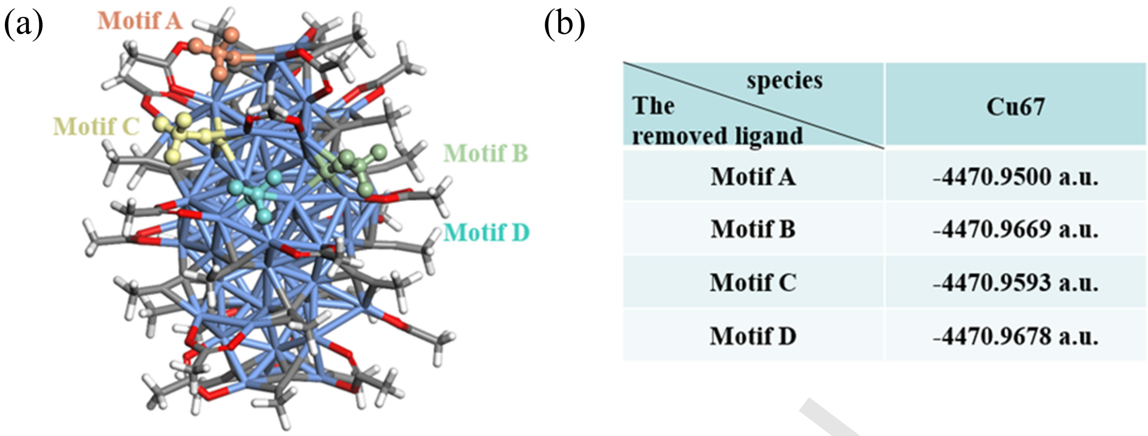

species The removed ligand	Cu67
Motif A	-4470.9500 a.u.
Motif B	-4470.9669 a.u.
Motif C	-4470.9593 a.u.
Motif D	-4470.9678 a.u.

Figure S20. (a) The different coordination environments of C≡C-CH_3 ligands in Cu_{67}; (b) The energy of Cu_{67} after the removal of a C≡C-CH_3 ligand. Color labels: Cu: blue; O: red; C: gray; H: white; Motif A: orange; Motif B: green; Motif C: yellow; Motif D: turquoise.

Figure S21. Possible pathways for the formation of ethylene (C_2H_4) on Cu_{67} at zero applied potential.

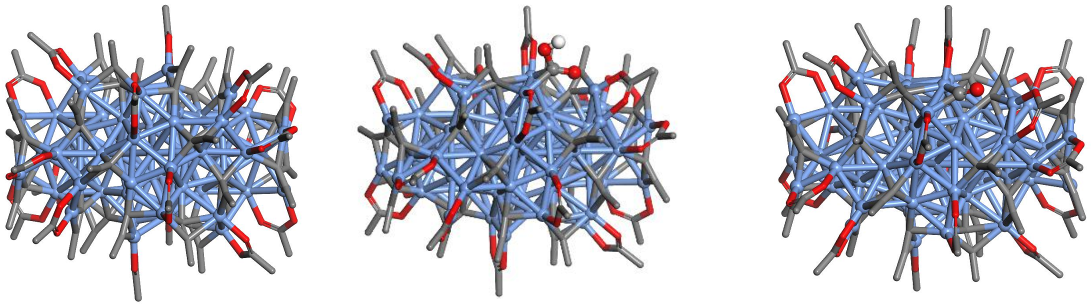

Cu$_{67}$* *COOH *CO

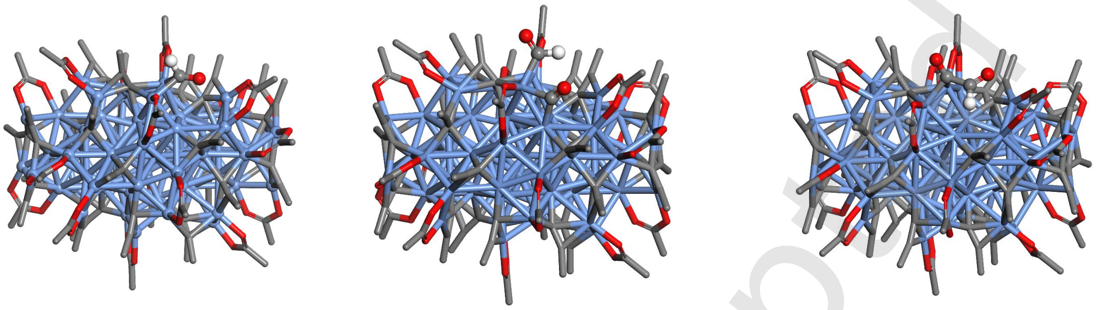

*CHO *CHO+*CO *COCHO

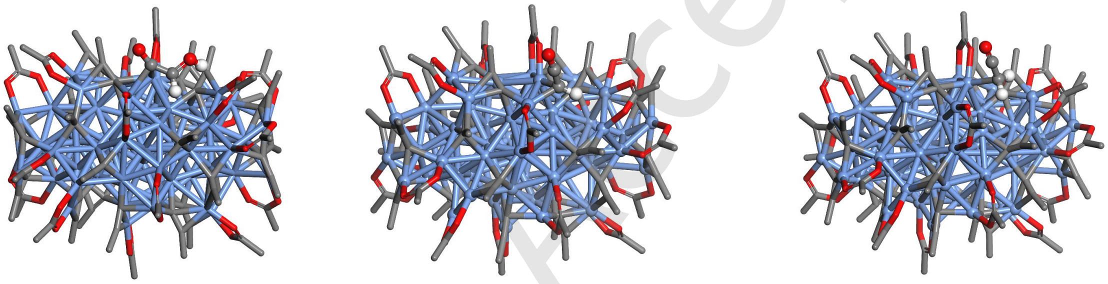

*COCHOH *CHCO *CH$_2$CO

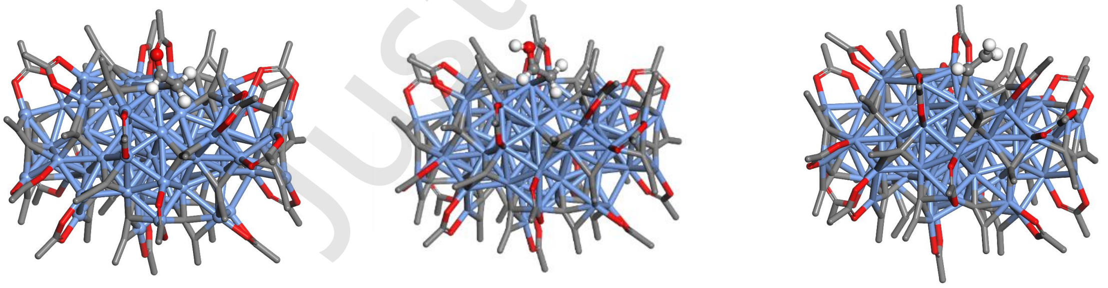

*CH$_2$CHO *CH$_2$CHOH *CHCH$_2$

Figure S22. The optimized structure of active sites on Cu$_{67}$ cluster, and the corresponding intermediate configurations to form CO and C$_2$H$_4$. Color labels: Cu: blue; O: red; C: gray; H: white.

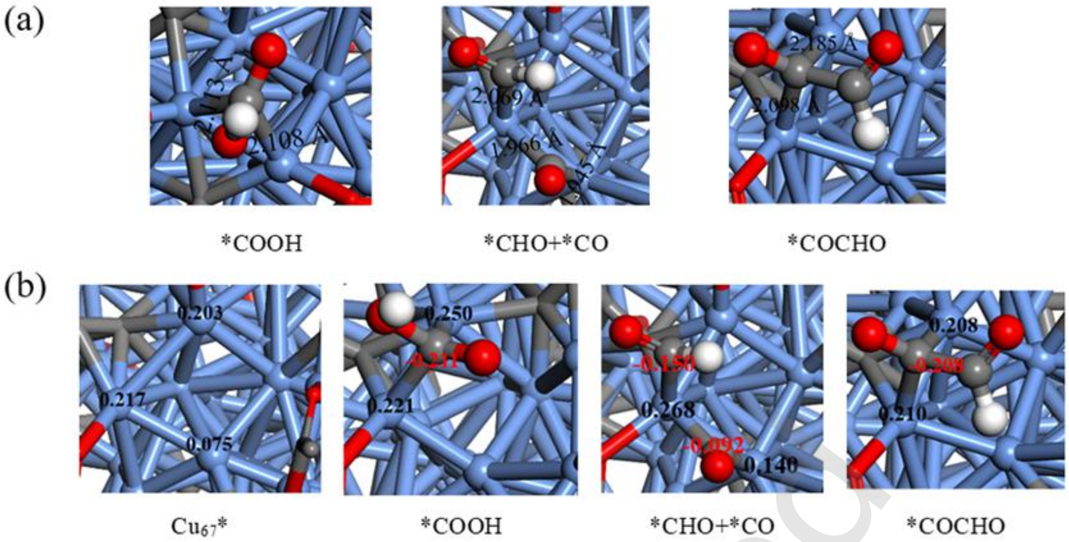

Figure S23. (a) Adsorption structures of *COOH, *CHO+*CO, and *COCHO intermediates on the Cu_{67} cluster (b) Hirshfeld charge analysis of the active Cu site in bare and the Cu active sites adsorbed with *COOH, *CHO+*CO and *COCHO structures.

Table S1. Crystal data and structure refinement of Cu_{67} nanocluster.

Compound	$[Cu_{67}(C{\equiv}CPh)_{24}(OAc)_{18}]^{-}$
CCDC No.	2417379
Formula	$C_{228}H_{174}Cu_{67}O_{36}$
Formula weight	7746.84
Temperature/K	149.99(10)
Crystal system	trigonal
Space group	P -3 1 c
a (Å)	19.5711(5)
b (Å)	19.5711(5)
c (Å)	37.4471(12)
α (°)	90
β (°)	90
γ (°)	120
V ($Å^3$)	12421.7(7)
Z	2
D_c / ($g \cdot cm^{-3}$)	2.071
Absorption coefficient	6.409 mm^{-1}
F(000)	7546
Radiation	Cu Kα (λ = 1.54184)
Theta (°) range	5.219 to 74.427
Index ranges	$-22 \leq h \leq 23$, $-24 \leq k \leq 20$, $-41 \leq l \leq 44$
Reflections collected	72407
Restraints	849
Parameters	578
Goodness-of-fit on F^2	0.997
R_{int}	0.0604
R_1/wR_2 [$I \geq 2\sigma(I)$]	0.0840/0.2358
R_1/wR_2 (all data)	0.1364/0.2842
Largest diff. peak/hole	0.668 / -0.603 e Å-3

Table S2. Comparison of Cu_{67} with other high-nuclearity (>50) Cu nanoclusters.

Cu nanocluster molecular formula	**Cu valence state**	**Cu core configuration**	**Main ligand coordination patterns**	**Major absorbance peak**	**Symmetry**	**Ref.**
$Cu_{67}(CCPh)_{24}(OAc)_{18}$	0-1	$Cu_5Cu_{26}Cu_{36}$		690 nm	C_3	This work
$[Cu_{61}(S^tBu)_{26}S_6Cl_6H_{14}]$	0-1	Not mentioned	Not mentioned	335nm, 440nm	Not mentioned	[8]
$[Cu_{58}H_{20}PET_{36}(PPh_3)_4]^{2+}$	+1	$Cu_8@Cu_6@Cu_{24}@Cu_{12}@Cu_8$	μ_4-$\eta^1, \eta^1, \eta^1, \eta^1$; μ_3-η^1, η^1, η^1	Not mentioned	C_2	[9]
$[Cu_{57}H_{20}PET_{36}(PPh_3)_4]^{+}$	+1	$Cu_8@Cu_6@Cu_{24}@Cu_{12}@Cu_7$	μ_4-$\eta^1, \eta^1, \eta^1, \eta^1$; μ_3-η^1, η^1, η^1; μ_2-η^1, η^1	Not mentioned	C_1	[9]
$[Cl@Cu_{70}H_{22}(CCPh)_{29}(CF_3COO)_{16}]^{2+}$	+1	$Cl@Cu_{16}@Cu_{43}@Cu_{11}$	μ_2-η^1, η^2; μ_3-η^1, η^1, η^2; μ_4-$\eta^1, \eta^1, \eta^2, \eta^2$; μ_4-$\eta^1, \eta^1, \eta^1, \eta^2$; μ_5-$\eta^1, \eta^1, \eta^1, \eta^1, \eta^2$	330 nm	C_1	[10]
$[Cu_{66}Cl_8(PPh_3)_8(SC_2H_5)_{32}H_{24}](SbF_6)_2$	+1	$Cu_{10}@Cu_{24}@Cu_{32}$	μ_4-$\eta^1, \eta^1, \eta^1, \eta^1$; μ_3-η^1, η^1, η^1	271.5 nm	C_4	[11]
$[(C_2)_8@Cu_{50}(mbo)_{20}(CF_3COO)_{14}(CH_3OH)_6 \cdot 2CH_3OH]$	+1	Not mentioned	μ_3-η^1, η^1, η^2; μ_3-η^1, η^2, η^2; μ_4-$\eta^1, \eta^1, \eta^1, \eta^2$	~400 nm	C_1	[12]
$[(C_2)_{10}@Cu_{56}(mbo)_{32}(CF_3COO)_4(DMF)_2]$[48]	+1	$Cu_{12}@Cu_{44}$	Not mentioned	~400 nm	C_2	[12]

Table S3. Coordinates for Cu_{67} NC.

Atom type symbol	X	Y	Z
Cu	14.034250	12.277750	8.236750
Cu	13.904500	14.422750	6.884750
Cu	12.507500	14.374750	4.750500
Cu	13.869500	10.039000	9.484500
Cu	16.497250	12.191000	7.830500
Cu	16.133250	9.598500	8.203000
Cu	13.863750	8.281000	11.266500
Cu	15.685000	10.319500	11.176750
Cu	11.550750	9.614750	10.444250
Cu	11.201500	7.556750	11.847000
O	14.457250	16.229250	6.143000
O	13.250000	16.123500	4.321500
O	18.174500	11.606000	7.063000
C	15.481500	13.803250	8.331000
C	14.057000	16.615000	5.084500
O	11.939000	5.756250	11.405500
C	16.582250	14.223250	8.095500

O	17.748750	9.466750	7.220250
C	15.456250	8.724750	9.890750
O	14.038500	6.351500	11.435500
C	16.187000	7.862250	9.505500
C	14.601500	17.984750	4.617000
H	13.883000	18.493750	4.190500
H	14.939000	18.480750	5.393000
H	15.330000	17.844500	3.977750
C	10.806250	13.242000	5.084500
C	13.158250	5.506500	11.390500
C	10.479000	14.263250	4.620750
C	17.058750	6.759750	9.434500
C	18.423750	10.420500	6.857250
C	9.532750	15.269750	4.183000
C	17.640250	15.161000	7.841000
C	9.788750	8.558250	10.743500
C	19.780500	10.201250	6.172750
H	20.370750	10.959500	6.368000
H	20.187500	9.376250	6.512250
H	19.650500	10.128250	5.205500
C	8.004750	6.837000	10.392000
C	9.086750	7.641750	10.646250
C	13.553500	4.058500	11.312000
H	12.960500	3.591250	10.688500
H	14.479250	3.989250	10.998250
H	13.479500	3.651000	12.201250
Cu	11.770750	13.557250	8.236750
Cu	9.978000	12.372250	6.884750
Cu	10.718000	11.186500	4.750500
Cu	13.792000	14.533750	9.484500
Cu	10.614250	15.733750	7.830500
Cu	13.041500	16.714500	8.203000
Cu	15.317250	15.408000	11.266500
Cu	12.641000	15.966000	11.176750
Cu	15.318750	12.738000	10.444250
Cu	17.275750	13.464250	11.847000
O	8.137000	11.947750	6.143000
O	8.832500	10.955000	4.321500
O	10.282250	17.478500	7.063000
C	9.726000	14.048000	8.331000
C	8.003250	11.408250	5.084500
O	18.466250	15.003500	11.405500
C	8.812000	14.791000	8.095500
O	12.347750	18.179500	7.220250

C	14.136750	16.565000	9.890750
O	16.901000	16.524000	11.435500
C	14.518250	17.629250	9.505500
C	6.544750	11.195000	4.617000
H	6.463250	10.318250	4.190500
H	5.946250	11.239000	5.393000
H	6.302000	11.896000	3.977750
C	12.549500	10.279500	5.084500
C	18.072750	16.184250	11.390500
C	11.828750	9.485500	4.620750
C	15.037250	18.935500	9.434500
C	11.184500	18.287250	6.857250
C	11.430250	8.162750	4.183000
C	7.470750	15.238500	7.841000
C	17.114500	11.740250	10.743500
C	10.696000	19.571750	6.172750
H	9.744000	19.704000	6.368000
H	11.206750	20.336750	6.512250
H	10.824000	19.495750	5.205500
C	19.497250	11.055750	10.392000
C	18.259250	11.590500	10.646250
C	19.129250	17.250500	11.312000
H	19.830250	16.970500	10.688500
H	18.726250	18.086750	10.998250
H	19.519250	17.390000	12.201250
Cu	11.794500	10.957250	8.236750
Cu	13.717000	9.997000	6.884750
Cu	14.374000	11.231000	4.750500
Cu	9.938000	12.219500	9.484500
Cu	10.487750	8.867500	7.830500
Cu	8.424750	10.479000	8.203000
Cu	8.418500	13.103250	11.266500
Cu	9.273250	10.506500	11.176750
Cu	10.730000	14.439500	10.444250
Cu	9.122250	15.771000	11.847000
O	15.005000	8.615000	6.143000
O	15.517250	9.713500	4.321500
O	9.142750	7.707500	7.063000
C	12.391750	8.941000	8.331000
C	15.539250	8.768750	5.084500
O	7.194250	16.032500	11.405500
C	12.205250	7.778000	8.095500
O	7.503000	9.145750	7.220250
C	8.006500	11.502250	9.890750

O	6.660000	13.916750	11.435500
C	6.894000	11.300750	9.505500
C	16.453250	7.612500	4.617000
H	17.253250	7.980250	4.190500
H	16.714250	7.072250	5.393000
H	15.967500	7.051750	3.977750
C	14.243750	13.270500	5.084500
C	6.368500	15.101250	11.390500
C	15.291750	13.043250	4.620750
C	5.503500	11.097000	9.434500
C	7.991250	8.084500	6.857250
C	16.636500	13.359500	4.183000
C	12.488500	6.392500	7.841000
C	10.696000	16.493500	10.743500
C	7.123000	7.019250	6.172750
H	7.484500	6.128750	6.368000
H	6.205000	7.079000	6.512250
H	7.124750	7.168000	5.205500
C	10.097500	18.899250	10.392000
C	10.253500	17.559750	10.646250
C	4.916750	15.483250	11.312000
H	4.808500	16.230250	10.688500
H	4.394000	14.716000	10.998250
H	4.600750	15.751000	12.201250
Cu	11.770750	10.971000	16.534250
Cu	9.978000	12.155750	17.886500
Cu	10.718000	13.341500	20.020500
Cu	13.792000	9.994250	15.286500
Cu	10.614250	8.794500	16.940500
Cu	13.041500	7.813500	16.568000
Cu	15.317250	9.120250	13.504500
Cu	12.641000	8.562250	13.594500
Cu	15.318750	11.790250	14.326750
Cu	17.275750	11.063750	12.924250
O	8.137000	12.580250	18.628000
O	8.832500	13.573000	20.449750
O	10.282250	7.049500	17.708000
C	9.726000	10.480250	16.440000
C	8.003250	13.119750	19.686500
O	18.466250	9.524500	13.365500
C	8.812000	9.737000	16.675750
O	12.347750	6.348500	17.551000
C	14.136750	7.963000	14.880250
O	16.901000	8.004250	13.335500

C	14.518250	6.898750	15.265500
C	6.544750	13.333250	20.154250
H	6.463250	14.210000	20.580500
H	5.946250	13.289000	19.378250
H	6.302000	12.632000	20.793500
C	12.549500	14.248500	19.686500
C	18.072750	8.343750	13.380500
C	11.828750	15.042500	20.150500
C	15.037250	5.592750	15.336750
C	11.184500	6.240750	17.913750
C	11.430250	16.365250	20.588000
C	7.470750	9.289750	16.930000
C	17.114500	12.787750	14.027500
C	10.696000	4.956250	18.598250
H	9.744000	4.824000	18.403000
H	11.206750	4.191250	18.258750
H	10.824000	5.032250	19.565500
C	19.497250	13.472250	14.379000
C	18.259250	12.937750	14.124750
C	19.129250	7.277750	13.459000
H	19.830250	7.557500	14.082500
H	18.726250	6.441250	13.772750
H	19.519250	7.138000	12.569750
Cu	11.794500	13.570750	16.534250
Cu	13.717000	14.531000	17.886500
Cu	14.374000	13.297250	20.020500
Cu	9.938000	12.308750	15.286500
Cu	10.487750	15.660500	16.940500
Cu	8.424750	14.049000	16.568000
Cu	8.418500	11.425000	13.504500
Cu	9.273250	14.021500	13.594500
Cu	10.730000	10.088500	14.326750
Cu	9.122250	8.757000	12.924250
O	15.005000	15.913000	18.628000
O	15.517250	14.814500	20.449750
O	9.142750	16.820500	17.708000
C	12.391750	15.587000	16.440000
C	15.539250	15.759250	19.686500
O	7.194250	8.495500	13.365500
C	12.205250	16.750000	16.675750
O	7.503000	15.382250	17.551000
C	8.006500	13.025750	14.880250
O	6.660000	10.611500	13.335500
C	6.894000	13.227500	15.265500

C	16.453250	16.915500	20.154250
H	17.253250	16.548000	20.580500
H	16.714250	17.456000	19.378250
H	15.967500	17.476500	20.793500
C	14.243750	11.257500	19.686500
C	6.368500	9.426750	13.380500
C	15.291750	11.484750	20.150500
C	5.503500	13.431000	15.336750
C	7.991250	16.443750	17.913750
C	16.636500	11.168500	20.588000
C	12.488500	18.135500	16.930000
C	10.696000	8.034500	14.027500
C	7.123000	17.509000	18.598250
H	7.484500	18.399500	18.403000
H	6.205000	17.449000	18.258750
H	7.124750	17.360000	19.565500
C	10.097500	5.629000	14.379000
C	10.253500	6.968250	14.124750
C	4.916750	9.044750	13.459000
H	4.808500	8.297750	14.082500
H	4.394000	9.812000	13.772750
H	4.600750	8.777000	12.569750
Cu	14.034250	12.250500	16.534250
Cu	13.904500	10.105500	17.886500
Cu	12.507500	10.153250	20.020500
Cu	13.869500	14.489250	15.286500
Cu	16.497250	12.337000	16.940500
Cu	16.133250	14.929500	16.568000
Cu	13.863750	16.247000	13.504500
Cu	15.685000	14.208500	13.594500
Cu	11.550750	14.913500	14.326750
Cu	11.201500	16.971500	12.924250
O	14.457250	8.298750	18.628000
O	13.250000	8.404500	20.449750
O	18.174500	12.922000	17.708000
C	15.481500	10.725000	16.440000
C	14.057000	7.913000	19.686500
O	11.939000	18.772000	13.365500
C	16.582250	10.305000	16.675750
O	17.748750	15.061250	17.551000
C	15.456250	15.803250	14.880250
O	14.038500	18.176500	13.335500
C	16.187000	16.666000	15.265500
C	14.601500	6.543250	20.154250

H	13.883000	6.034250	20.580500
H	14.939000	6.047250	19.378250
H	15.330000	6.683750	20.793500
C	10.806250	11.286000	19.686500
C	13.158250	19.021500	13.380500
C	10.479000	10.264750	20.150500
C	17.058750	17.768250	15.336750
C	18.423750	14.107500	17.913750
C	9.532750	9.258250	20.588000
C	17.640250	9.367000	16.930000
C	9.788750	15.969750	14.027500
C	19.780500	14.327000	18.598250
H	20.370750	13.568500	18.403000
H	20.187500	15.151750	18.258750
H	19.650500	14.399750	19.565500
C	8.004750	17.691000	14.379000
C	9.086750	16.886250	14.124750
C	13.553500	20.469500	13.459000
H	12.960500	20.936750	14.082500
H	14.479250	20.538750	13.772750
H	13.479500	20.877000	12.569750
Cu	12.533250	12.264000	6.097250
Cu	12.533250	12.264000	10.390750
Cu	12.533250	12.264000	18.673750
Cu	12.533250	12.264000	14.380250
Cu	13.385500	13.740500	12.385500
Cu	10.828250	12.264000	12.385500
Cu	13.385500	10.787500	12.385500
H	8.470750	14.898500	4.367000
H	9.678000	15.469500	3.070000
H	9.705000	16.233250	4.767750
H	16.613000	13.690750	3.092500
H	17.296500	12.435750	4.285750
H	17.057500	14.201000	4.826750
H	11.960250	7.377000	4.816750
H	11.715000	8.023000	3.088000
H	10.302250	8.047500	4.300000
H	17.646750	15.436000	6.734750
H	18.640250	14.691000	8.121500
H	17.473500	16.100500	8.465000
H	19.741750	11.173500	9.284750
H	19.496750	9.949250	10.665500
H	20.281500	11.600750	11.014500
H	12.164250	6.126750	6.781000

H	11.918500	5.745250	8.586250
H	13.607500	6.206500	7.954000
H	15.310250	19.177500	8.354500
H	15.968500	19.010500	10.087750
H	14.253500	19.676250	9.803500
H	15.044500	5.129500	14.295000
H	14.386250	4.962250	16.028500
H	16.101500	5.628250	15.744000
H	17.273000	6.514500	8.342000
H	16.574000	5.859000	9.938000
H	18.035000	7.012500	9.965750
H	6.741500	14.384000	8.036500
H	7.381250	15.573500	6.755000
H	7.224750	16.112750	8.529750
H	5.263750	10.015000	9.701750
H	5.141000	11.316250	8.376000
H	4.979250	11.794750	10.168000
H	8.228250	5.777000	10.746500
H	7.794000	6.826750	9.271750
H	7.093500	7.239000	10.946500
H	10.733250	5.336500	15.279000
H	10.428500	5.028250	13.468500
H	9.001000	5.409500	14.601000
H	10.098500	8.359000	21.001500
H	8.891250	8.930250	19.704500
H	8.864000	9.693750	21.402250
H	7.182250	17.076500	14.874500
H	7.616500	18.126250	13.399750
H	8.317000	18.538750	15.074500
H	9.375250	19.348500	11.151000
H	9.680000	19.040250	9.340500
H	11.107500	19.421500	10.473000
H	17.365000	11.333750	19.727000
H	16.681500	10.078750	20.920250
H	16.920500	11.844000	21.461250
H	18.193750	9.145750	15.958250
H	17.200000	8.400750	17.345000
H	18.366750	9.810250	17.688500
H	10.691500	16.273500	21.451250
H	10.936500	16.919250	19.722500
H	12.349500	16.944000	20.934500
H	17.315250	18.118500	14.282500
H	18.014000	17.463000	15.878750
H	16.553000	18.616500	15.906250

H	12.962500	18.602500	16.004500
H	13.208500	18.221000	17.809750
H	4.992250	12.459000	15.642250
H	5.115000	13.760500	14.316750
H	5.276750	14.238750	16.108500
H	19.938250	13.886000	13.412750
H	20.183250	12.661500	14.793500
H	19.398500	14.313250	15.142500
H	7.490250	8.198500	17.260000
H	6.850500	9.388000	15.978500
H	7.007000	9.927500	17.753250
H	11.519250	18.682250	17.177500

References

[1] VandeVondele, J.; Krack, M.; Mohamed, F.; Parrinello, M.; Chassaing, T.; Hutter, J. Quickstep: Fast and Accurate Density Functional Calculations Using a Mixed Gaussian and Plane Waves Approach. *Comput. Phys. Commun.* **2005**, *167*, 103–128.

[2] Perdew, J. P.; Burke, K.; Ernzerhof, M. Generalized Gradient Approximation Made Simple. *Phys. Rev. Lett.* **1996**, *77*, 3865–3868.

[3] Grimme, S.; Antony, J.; Ehrlich, S.; Krieg, H. A Consistent and Accurate Ab Initio Parametrization of Density Functional Dispersion Correction (DFT-D) for the 94 Elements H-Pu. *J. Chem. Phys.* **2010**, *132*, 154104.

[4] Grimme, S.; Ehrlich, S.; Goerigk, L. Effect of the Damping Function in Dispersion Corrected Density Functional Theory. *J. Comput. Chem.* **2011**, *32*, 1456–1465.

[5] Nørskov, J. K.; Rossmeisl, J.; Logadottir, A.; Lindqvist, L.; Kitchin, J. R.; Bligaard, T.; Jónsson, H. Origin of the Overpotential for Oxygen Reduction at a Fuel-Cell Cathode. *J. Phys. Chem. B* **2004**, *108*, 17886–17892.

[6] Peterson, A. A.; Abild-Pedersen, F.; Studt, F.; Rossmeisl, J.; Nørskov, J. K. How Copper Catalyzes the Electroreduction of Carbon Dioxide into Hydrocarbon Fuels. *Energy Environ. Sci.* **2010**, *3*, 1311–1315.

[7] Tang, Q.; Lee, Y.; Li, D.-Y.; Choi, W.; Liu, C. W.; Lee, D.; Jiang, D. Lattice-Hydride Mechanism in Electrocatalytic CO2 Reduction by Structurally Precise Copper-Hydride Nanoclusters. *J. Am. Chem. Soc.* **2017**, *139*, 9728–9736.

[8] Sagadevan, A.; Ghosh, A.; Maity, P.; Mohammed, O. F.; Bakr, O. M.; Rueping, M. Visible-Light Copper Nanocluster Catalysis for the C–N Coupling of Aryl Chlorides at Room Temperature. *J. Am. Chem. Soc.* **2022**, *144*, 12052–12061.

[9] Dong, C.; Huang, R.; Sagadevan, A.; Yuan, P.; Gutiérrez - Arzaluz, L.; Ghosh, A.; Nematulloev, S.; Alamer, B.; Mohammed, O. F.; Hussain, I.; Rueping, M.; Bakr, O. M. Isostructural Nanocluster Manipulation Reveals Pivotal Role of One Surface Atom in Click Chemistry. *Angew. Chem. Int. Ed.* **2023**, *62*, e202307140.

[10] Qin, H.-N.; He, M.-W.; Wang, J.; Li, H.-Y.; Wang, Z.-Y.; Zang, S.-Q.; Mak, T. C. W. Thiacalix[4]Arene Etching of an Anisotropic $Cu_{70}H_{22}$ Intermediate for Accessing Robust Modularly Assembled Copper Nanoclusters. *J. Am. Chem. Soc.* **2024**, *146*, 3545–3552.

[11] Sun, X.; Wang, Y.; Wu, Q.; Han, Y.; Gong, X.; Tang, X.; Aikens, C. M.; Shen, H.; Zheng, N. Cu_{66} Nanoclusters from Hierarchical Square Motifs: Synthesis, Assembly, and Catalysis. *Aggregate* **2024**, *6*, e651.

[12] Han, B.-L.; Alkan, F.; Yuan, Z.-R.; Mahato, P.; Wang, Z.; Tung, C.-H.; Sun, D. Hydrogen-Bonding-Assisted Assembly of Stable High-Nuclearity Copper(I)-Alkyne Nanoclusters for X-Ray Scintillation. *Angew. Chem. Int. Ed.* **2025**, *25*, e202507412.

Address correspondence to Zhenghua Tang, zhht@scut.edu.cn; Qing Tang, qingtang@cqu.edu.cn; Likai Wang, lkwangchem@sdut.edu.cn